TMEM135 is an LXR-Inducible Regulator of Peroxisomal Metabolism

Benjamin J. Renquist[1], Thushara W. Madanayake[1], Susma Ghimire[1], Caroline E. Geisler[1], Yafei Xu[1], Randy L. Bogan*[1]

[1]School of Animal & Comparative Biomedical Sciences, College of Agriculture & Life Sciences, University of Arizona, Tucson, Arizona, 85721, USA

*Address correspondence to:

Randy L. Bogan, PhD, MCR
School of Animal and Comparative Biomedical Sciences
University of Arizona
PO Box 210090
Tucson, AZ 85721-0090
Phone: 520-621-1487
Fax: 520-621-9435
Email: boganr@email.arizona.edu

Summary

The liver x receptors (LXRs) are key regulators of systemic lipid metabolism. We identified transmembrane protein 135 (TMEM135), a peroxisomal protein with an unknown function, as an LXR target gene. The LXRs induce *TMEM135* transcription in humans via an LXR response element located downstream of the putative transcriptional start site, but do not increase *Tmem135* in murine cells. Functionally, knockdown of TMEM135 in hepatocytes *in vitro* and *in vivo* results in fatty acid accumulation due to reduced peroxisomal β-oxidation, which was most pronounced with elevated fatty acid loading. Mechanistically, proteomic and Western blot analyses indicated that TMEM135 mediates import of peroxisome matrix proteins necessary for β-oxidation and bile acid synthesis. These findings indicate that the LXRs regulate peroxisomal metabolism via transcriptional control of *TMEM135*, and TMEM135 mediates an auxiliary matrix protein import pathway and thus may serve as a therapeutic target for metabolic and aging disorders associated with peroxisome dysfunction.

Keywords: peroxisome, liver x receptors, nuclear receptors, lipid metabolism, β-oxidation, liver metabolism, steatosis, fatty acid metabolism, cholesterol, bile acid synthesis

Introduction

The liver x receptors (LXR) α (NR1H3) and β (NR1H2) belong to the nuclear receptor superfamily and are key regulators of cholesterol and fatty acid metabolism (Hong and Tontonoz, 2014). Oxysterols are natural LXR ligands (Peet et al., 1998) that increase during cholesterol loading. The LXRs heterodimerize with the retinoic acid receptor (RXR) and bind to LXR response elements (LXRE) within the promoters of target genes (Peet et al., 1998). The LXREs belong to the direct repeat 4 (DR4) class that consist of two hexanucleotide half-sites separated by a 4-nucleotide spacer (Teboul et al., 1995; Willy et al., 1995). The protein products of known LXR target genes affect systemic lipid metabolism. Well known examples include increasing cholesterol efflux via ATP-binding cassette (ABC) sub-family A, member 1 (ABCA1) (Costet et al., 2000), and sub-family G, member 1 (ABCG1) (Kennedy et al., 2001); limiting cholesterol

uptake via induction of myosin regulatory light chain interacting protein (MYLIP) that targets the low-density lipoprotein receptor (LDLR) for ubiquitin-mediated degradation (Zelcer et al., 2009); and increased lipogenesis via induction of sterol regulatory element binding protein 1c (SREBP1c, encoded by sterol regulatory element binding transcription factor 1 gene or *SREBF1*) (Repa et al., 2000; Yoshikawa et al., 2001). Also, the *NR1H3* isoform of the LXRs is itself an LXR target gene (Laffitte et al., 2001; Whitney et al., 2001), leading to auto-amplification of LXR actions in certain species and tissues. Although many LXR target genes have been discovered, additional target genes may remain unidentified.

We have previously investigated LXR actions within the steroidogenic corpus luteum of the ovary (Seto and Bogan, 2015; Xu et al., 2018a; Xu et al., 2018b). To uncover novel LXR target genes, rhesus macaque luteal cells were treated with vehicle or 1 μM T0901317 (T09, synthetic LXR agonist) for 24 hours, mRNA were isolated and used for microarray analysis of gene expression on the Affymetrix® Rhesus Macaque genome chip (unpublished data). Genes that were differentially expressed (>2-fold change in T09 vs vehicle, $p < 0.05$ with Benjamini and Hochberg correction for false discovery rate) were identified. Several known LXR target genes were differentially expressed including *ABCA1*, *ABCG1*, *NR1H3*, *SREBF1*, and *MYLIP*. One gene that was differentially expressed and not previously determined to be an LXR target gene was transmembrane protein 135 (*TMEM135*). Therefore, the objective of the current study is to determine if *TMEM135* is an LXR target gene and to identify its physiologic role in lipid metabolism.

Results

LXR Agonist Increases Expression of TMEM135 in Human Hepatocyte and Macrophage Cell Lines

Macrophage and hepatocyte cell lines were selected for initial studies on LXR regulation of *TMEM135* transcription as these cell types play a pivotal role in LXR-mediated reverse cholesterol transport from peripheral tissues to the liver (Hong and Tontonoz, 2014). The LXR

ligand T09 increased the mRNA expression of *TMEM135* in both HepG2 (Figure 1A) and Hep3B (Figure 1B) hepatocyte cell lines, with an approximately 2-fold maximum increase in HepG2 cells and a 3-fold increase in Hep3B cells. In monocyte-derived macrophages (THP-1), T09 also induced *TMEM135* mRNA expression up to 4-fold (Figure 1C). The protein synthesis inhibitor cycloheximide was used to determine whether the effect of T09 on *TMEM135* in THP-1 cells requires synthesis of new proteins. Cycloheximide did not significantly affect basal or T09-stimulated *TMEM135* mRNA expression (Figure 1D), indicating that T09 induces *TMEM135* via a direct transcriptional mechanism not involving the synthesis of intermediary proteins. As TMEM135 has previously been reported to be localized to mitochondria (Exil et al., 2010; Lee et al., 2016), the effect of T09 on TMEM135 protein expression in mitochondria/peroxisome-enriched fractions from HepG2 cells was determined. Relative concentrations of TMEM135 were significantly ($p < 0.05$) increased approximately 1.8-fold following a 24-hour T09 treatment (Figure 1E and 1F).

<u>A LXRE Downstream of the Putative Transcription Start Site Mediates LXR Agonist Induction of *TMEM135*</u>

A 4 kb region spanning from -3319 to +682 bp (relative to the transcriptional start site) of the human *TMEM135* promoter was analyzed with MatInspector (Cartharius et al., 2005) for potential LXRE binding sites. This analysis yielded three potential LXREs (Figure S1), and these were arbitrarily designated LXRE1, LXRE2 and LXRE3 in order from most distal to most proximal to the translation start site. Electrophoretic mobility shift assays (EMSA) were used to determine if LXR/RXR heterodimers bind these LXREs. As shown in Figure 2A, NR1H3 and RXRA nuclear receptors together, but not individually, caused a shift in mobility of the fluorescent LXRE1 probe indicating that NR1H3/RXRA heterodimers bind the LXRE1 sequence in the *TMEM135* promoter. A 200-fold molar excess of unlabeled LXRE1, LXRE2, and LXRE3 oligonucleotides eliminated the appearance of the shifted fluorescent band while the same molar excess of mutant LXRE1, LXRE2, and LXRE3 oligonucleotides (Figure S1B) did not prevent NR1H3/RXRA binding to the

fluorescent probe; which validated the specificity of NR1H3/RXRA heterodimer binding to all 3 LXREs in the *TMEM135* promoter (Figure 2A). Similar results were obtained for NR1H2/RXRA heterodimers (Figure 2B), indicating that both LXR isoforms specifically bind to all 3 LXRE sites in the *TMEM135* promoter. The LXRE1 and LXRE2 sites have identical hexanucleotide half-sites, whereas the LXRE3 site is unique (Figure S1B). To indicate if these sequence variations may cause differences in relative binding affinity, a fluorescent LXRE3 probe was incubated with NR1H3/RXRA heterodimers and increasing concentrations (from 0.25 to 10-fold molar excess) of either LXRE1 or LXRE3 unlabeled competitor DNA. Oligonucleotides with the LXRE3 sequence more effectively inhibited binding to the fluorescent probe than oligonucleotides with the LXRE1 sequence (Figure 2C). As a complementary approach, because the LXRE1 and LXRE3 sites were fluorescently labelled with spectrally distinct fluorophores, an EMSA was performed where a mixture of fluorescent LXRE1 and LXRE3 probes were incubated with increasing concentrations of NR1H3/RXRA heterodimers. This approach resulted in a higher percentage of LXRE3 than LXRE1 bound across a range of NR1H3/RXRA heterodimer concentrations (Figure 2D). Collectively, this indicates that LXRE3 has a higher binding affinity for NR1H3/RXR heterodimers than LXRE1.

Luciferase reporter assays were used to study transcription initiation from the *TMEM135* promoter. Transfection of HepG2 cells with wild type *TMEM135* promoter/pGL 4.17 resulted in a large increase in luciferase expression that was responsive to T09 as compared to the empty pGL 4.17 vector (Figure 2E). Furthermore, luciferase activity was further amplified by co-transfection of plasmids that constitutively express NR1H3 and RXRA (Figure 2E). Next, we determined the requirement of each individual LXRE to LXR agonist-induced transcription from the *TMEM135* promoter. Promoters containing all combinations of wild type and mutant LXREs (Figure S1B) were generated, and T09-induced luciferase activity was determined. LXR-agonist induced luciferase activity was significantly ($p < 0.05$) higher in cells transfected with the wild type *TMEM135* promoter as compared to the *TMEM135* promoter with all 3 LXREs mutated (Figure

2F). Furthermore, constructs containing the wild type LXRE3 site and mutated LXRE1 and/or LXRE2 sites were not significantly different from the wild type promoter, while all constructs that contained a mutated LXRE3 were not significantly different from the promoter that had all three LXREs mutated (Figure 2F). This indicates that even though all 3 LXREs bind LXR/RXR heterodimers, the LXRE3 site alone mediates LXR agonist-induced transcription from the *TMEM135* promoter.

We next determined whether *Tmem135* mRNA expression was induced by T09 in mice. The murine LXRE3 site showed relatively little homology with the human sequence as a total of 3 nucleotides within both hexanucleotide half-sites were unique in mice (Figure S2A). In mouse hepatocyte (BNL 1NG A.2) and macrophage (RAW 264.7) cell lines, T09 did not significantly induce *Tmem135* mRNA expression (Figure S2B) whereas it did increase the known LXR target gene *Abca1* (Figure S2C). These data indicate that *Tmem135* is not an LXR target gene in mice.

<u>*TMEM135* is a Direct Target Gene of the LXRs</u>

To directly determine whether the LXRs are needed for T09-induced *TMEM135* transcription, siRNA-mediated knockdown of the LXRs was performed in HepG2 cells. The *NR1H2* siRNA caused an approximately 75% decrease ($p < 0.05$) in *NR1H2* mRNA expression compared to the control and *NR1H3* siRNA groups (Figure 3A). The *NR1H3* siRNA resulted in an approximately 70-80% decrease ($p < 0.05$) in *NR1H3* mRNA expression compared to the control siRNA depending on the presence or absence of T09 (Figure 3B). The *NR1H2* siRNA by itself also caused a significant reduction in T09-stimulated *NR1H3* mRNA expression and tended to slightly improve *NR1H3* knockdown when co-transfected with the *NR1H3* siRNA (Figure 3B). Decreased *NR1H3* mRNA expression is expected to occur following NR1H2 knockdown because *NR1H3* itself is an LXR target gene (Kennedy et al., 2001; Whitney et al., 2001). Consistent with *NR1H3* being an LXR target gene, T09 induced a significant increase in *NR1H3* in the control siRNA group, while T09 was not as effective at inducing *NR1H3* in the *NR1H2* siRNA group (Figure 3B).

The known LXR target gene *ABCA1* was significantly increased by T09 in the control siRNA group, and the effect of T09 was completely abolished by *NR1H2/NR1H3* siRNA co-transfection (Figure 3C). Also, *NR1H3* knockdown alone significantly inhibited the T09-induced increase in *ABCA1* (Figure 3C). Results for *TMEM135* were very similar to *ABCA1* with T09 causing a significant increase in the control siRNA group, and the effect of T09 was completely blocked by *NR1H2/NR1H3* siRNA co-transfection (Figure 3D). Furthermore, *NR1H3* knockdown itself significantly inhibited the T09-induced increase in *TMEM135* as compared to the control siRNA (Figure 3D).

The LXRE3 site of the human *TMEM135* promoter lies downstream of the putative transcriptional start site, but before the translation initiation site (Figure S1). To determine whether LXR-mediated transcription of *TMEM135* results in an mRNA with a truncated 5' UTR, primers and a probe were designed to amplify and detect a 76 base pair region encompassing the LXRE3 site in the 5' UTR. There was a significant ($p < 0.05$) reduction in mRNA expression of full-length 5' UTR transcripts caused by T09 in the control siRNA group, while this effect was blocked by *NR1H2/NR1H3* siRNA co-transfection (Figure 3E). Furthermore, *NR1H2/NR1H3* co-knockdown resulted in a significant ($p < 0.05$) increase in basal mRNA expression of full-length 5' UTR transcripts compared to all other groups (Figure 3E). ChIP was used to determine if the reduction in full-length 5' UTR transcripts is associated with increased NR1H2 and/or NR1H3 binding to the LXRE3 site on the *TMEM135* gene. Monoclonal antibodies specific for each LXR isoform were used for ChIP, and QPCR of the LXRE3 region on chromatin purified via ChIP indicated that T09 treatment caused a significant increase in binding of NR1H3 to LXRE3 in the *TMEM135* gene (Figure 3F). This indicates that LXR binding to LXRE3 increases mRNA expression of *TMEM135* via a transcript with a truncated 5' UTR relative to the putative mRNA sequence.

<u>TMEM135 Mediates Fatty Acid Metabolism and Proliferation in HepG2 Cells</u>

To begin unraveling the biologic function of TMEM135, a series of knockdown experiments were performed. Transfection of HepG2 cells with siRNA against *TMEM135* decreased its mRNA

expression by 70-90%. As TMEM135 has previously been implicated in fat metabolism (Exil et al., 2010), and the LXRs are known to induce lipogenesis (Hong and Tontonoz, 2014), we first determined its effect on triglycerides and mRNA expression of fatty acid oxidation and lipogenesis-associated genes. Knockdown of TMEM135 significantly increased basal triglyceride accumulation in HepG2 cells (Figure 4A). Furthermore, T09 significantly increased intracellular triglyceride concentrations, while TMEM135 knockdown further increased triglyceride accumulation in the presence of T09 (Figure 4A). An increase in triglyceride accumulation could result from a decrease in fatty acid oxidation and/or an increase in lipogenesis. There were no significant effects of TMEM135 knockdown on mRNA expression of the key regulator of fatty acid β-oxidation, peroxisome proliferator activated receptor alpha (*PPARA*), while it tended to increase the PPARA target gene carnitine palmitoyltransferase 1A (*CPT1A*) (Kersten and Stienstra, 2017) (Figure 4B). It is known that the LXRs induce lipogenesis via induction of SREBP1c (*SREBF1* gene) (Repa et al., 2000; Yoshikawa et al., 2001). As expected, T09 caused a significant increase in *SREBF1* and the SREBP1c/LXR target gene fatty acid synthase (*FASN*) (Figure 4B), consistent with the T09-induced increase in triglyceride accumulation (Figure 4A). However, TMEM135 knockdown significantly suppressed both basal and T09-induced *SREBF1* mRNA expression (Figure 4B). This indicates that the increase in triglyceride accumulation in HepG2 cells occurred despite an apparent reduction in lipogenesis. Thus, an inhibition of fatty acid oxidation seems a more likely explanation for the increase in triglycerides. The tendency for an increase in *CPT1A* mRNA caused by TMEM135 knockdown is not evidence against a decrease in fatty acid oxidation because reduced β-oxidation would result in fatty acid accumulation, and because fatty acids are the endogenous ligands for PPARA (Kersten and Stienstra, 2017), this would also cause increased *CPT1A* mRNA expression. Further supporting an impairment in fatty acid β-oxidation, TMEM135 knockdown significantly reduced ATP concentrations when HepG2 cells were incubated in glucose-free medium (Figure 4C).

During these experiments it appeared that TMEM135 knockdown also inhibited replication of HepG2 cells. Because enhanced β-oxidation is a hallmark of hepatocellular carcinoma (HCC) (Beyoglu and Idle, 2013) and our previous experiments indicated a key role for TMEM135 in fatty acid metabolism, we determined whether TMEM135 regulated proliferation of HepG2 cells. Knockdown of *TMEM135* significantly ($p < 0.05$) reduced viable HepG2 cell numbers at 48 and 72 hours post-transfection as compared to cells transfected with the control siRNA (Figure 4D). Cell cycle analysis indicated that *TMEM135* knockdown significantly ($p < 0.05$) increased the percentage of HepG2 cells in the G0/G1 stage, with a corresponding significant reduction in the percentage of cells in the S phase (Figure 4E). The increase in G0/G1 arrest was associated with alterations in mRNA expression of tumor suppressor and cell cycle genes. There were significant increases in cyclin dependent kinase inhibitor 2A (*CDKN2A*) and tumor protein p53 (*TP53*) (Figure 4F), which restrict passage through the G1/S checkpoint (LaPak and Burd, 2014). There were also significant increases in cyclin dependent kinase 2 (*CDK2*) and cyclin E1 (*CCNE1*) (Figure 4F), which increase prior to passage through the G1/S checkpoint, but no change in cyclin A2 (*CCNA2*) (Figure 4F) which is increased in the S phase (Harper and Adams, 2001). Collectively, these data indicate that TMEM135 knockdown reduces HepG2 proliferation by restricting passage through the G1/S checkpoint.

<u>Liver-Selective TMEM135 Knockdown Reduces Peroxisomal β-Oxidation</u>

To determine the physiologic function of TMEM135, a siRNA knockdown experiment was performed in male C57BL/6 mice. Mice received either a non-targeting control or *Tmem135* siRNA and were sacrificed 4 days later in either the *ad libitum* fed state or after a 12-hour fast. Because we determined that *Tmem135* is not an LXR target gene in mice (Figure S2), we used fasting to induce hepatic fat accumulation. The *Tmem135* siRNA caused an approximately 60% mRNA knockdown in the liver while no knockdown was observed in other tissues including skeletal muscle, adipose, and heart (Figure 5A). Knockdown of TMEM135 in the liver was further confirmed by Western blot and proteomic analysis of mitochondria/peroxisome-enriched fractions

(Figure 5B). Fed mice injected with the *Tmem135* siRNA gained significantly less weight during the 4-day treatment, while the loss in weight from fasting was similar for both siRNAs (Figure 5C). There was no significant effect of the *Tmem135* siRNA on basal or fasting-induced hepatic triglycerides (Figure S3A), while there was a tendency for increased hepatic non-esterified fatty acid (NEFA) concentrations in TMEM135 knockdown mice in the fed state (Figure S3B). There were no significant effects of TMEM135 knockdown on liver ATP or glycogen concentrations (Figure S3C-D). Also, there were no significant effects of TMEM135 on serum lipids (total cholesterol, HDL cholesterol, triglycerides), although there was a trend for fasting to reduce serum triglycerides in control siRNA mice that was not observed in TMEM135 knockdown mice (Figure S4A). There were no significant effects of TMEM135 knockdown on serum NEFA, glucose, insulin, or β-hydroxybutyrate concentrations (Figure S4B-E). The mRNA expression of key genes involved in fatty acid β-oxidation were determined in the liver. As expected, fasting significantly induced mRNA expression of *Ppara*, *Cpt1a*, acyl-CoA dehydrogenase medium chain (*Acadm*), uncoupling protein 2 (*Ucp2*), and sirtuin 3 (*Sirt3*) (Figure 5D). Similarly, knockdown of TMEM135 significantly increased *Acadm* and *Sirt3* in fed animals, while *Ucp2* was significantly reduced by TMEM135 knockdown in fasted animals (Figure 5D). As expected with increased β-oxidative flux, fasting significantly increased NADH in animals receiving the control siRNA, while TMEM135 knockdown significantly reduced NADH (Figure 5E) indicating an impairment in β-oxidation in fasted mice. Reduced hepatic NADH during fasting could be due to reduced β-oxidation in peroxisomes and/or mitochondria. However, there was a reciprocal significant increase in hepatic ketone concentrations in fasted mice with TMEM135 knockdown (Figure 5F). Because ketogenesis occurs exclusively in mitochondria and is intricately linked with fatty acid oxidation (Newman and Verdin, 2017), this indicates that mitochondrial fatty acid β-oxidation was not impaired. Thus, knockdown mice have impaired fatty acid β-oxidation in peroxisomes but not mitochondria.

<u>TMEM135 Knockdown Reduces Import of Peroxisome Matrix Enzymes</u>

TMEM135 is a peroxisomal protein with high homology to the Tim17 family that mediate translocation of proteins across mitochondrial membranes (Zarsky and Dolezal, 2016). In addition to peroxisomes, TMEM135 has been reported to be localized to mitochondria (Exil et al., 2010; Lee et al., 2016). Therefore, we hypothesized that TMEM135 mediates protein import into peroxisomes and/or mitochondria. A mitochondria/peroxisome-enriched fraction was prepared from frozen mouse livers. This fraction was validated to contain both mitochondria and peroxisomes as indicated by presence of the mitochondria marker cytochrome c oxidase subunit 4I1 (COX4I1) and the peroxisome marker ATP binding cassette subfamily D member 3 (ABCD3, also known as PMP70), while COX4I1 and ABCD3 were not detected in the cytosolic fraction (Figure 6A). Furthermore, the cytosolic protein tubulin beta class I (TUBB) segregated to the cytosolic fraction and was not detected in the mitochondria/peroxisome-enriched fraction. Proteomic analysis of a subset of fed mice was used to provide an unbiased estimate of differential protein abundance in the mitochondria/peroxisome-enriched fractions. A total of 23 proteins were significantly less abundant (Fisher's Exact Test, $p < 0.05$) in the mitochondria/peroxisome-enriched fraction from TMEM135 knockdown livers (Figure 6B). Interestingly, these 23 proteins included nearly all the matrix proteins known to be necessary for peroxisomal bile acid synthesis and β-oxidation of very-long chain fatty acids, branched chain fatty acids, and dicarboxylic acids (Baes and Van Veldhoven, 2016; Waterham et al., 2016) (Figure 6 C-D). Analysis of ABCD3 expression by proteomic and Western blot analysis demonstrated that total peroxisome content was not significantly altered by TMEM135 knockdown (Figure 6E), indicating that the lower abundance of peroxisomal proteins in the proteomic data was not simply due to reduced peroxisome content. Four peroxisomal proteins were selected for further analysis via Western blot: acetyl-CoA acyltransferase 1 (ACAA1), acyl-CoA oxidase 1 (ACOX1), sterol carrier protein 2 (SCP2), and catalase (CAT). All these proteins were enriched in the mitochondria/peroxisome fraction, but except for SCP2 (which had low detection sensitivity) each protein was also clearly detectable in the cytosolic fraction (Figure 6F). This contrasts with

the peroxisome membrane protein ABCD3 which appeared to be exclusively localized to the mitochondria/peroxisome fraction (Figure 6A). Collectively, detection of these proteins in the cytoplasm indicates that their import into peroxisomes may be rate-limiting.

We next used Western blot to quantitatively determine import of ACAA1, ACOX1, SCP2, and CAT into peroxisomes. Whole cell lysates (using TUBB as loading control) and mitochondria/peroxisome-enriched fractions (using ABCD3 as loading control for peroxisomes) were analyzed (Figure 7A). The signal for each protein was normalized to the respective loading control, and the ratio of peroxisome to whole cell lysate was used to determine import. Using this method, there were no significant differences between siRNAs for peroxisome import of ACOX1 and CAT in either fed or fasted animals (Figure 7B). However, relative ACAA1 import was significantly reduced in TMEM135 knockdown mice when fasted (Figure 7B). Furthermore, SCP2 import was significantly lower in TMEM135 knockdown mice in both the fed and fasted state (Figure 7B). Collectively, Western blot confirmed that TMEM135 mediates the import of ACAA1 and SCP2 into peroxisomes, and thus may mediate the import of additional proteins identified via proteomics.

TMEM135 Knockdown Inhibits Fasting-Induced β-Oxidation

We next determined the effect of TMEM135 on markers of peroxisome function. In fasted mice, TMEM135 knockdown resulted in a significant increase in total fatty acids and linoleic acid, with trends ($0.05 < p < 0.1$) for increases in several other fatty acids (Figure 7C-D). In general, mitochondria preferentially oxidize short and medium chain fatty acids (<C12), both mitochondria and peroxisomes oxidize long chain fatty acids (C14-C18), while peroxisomes exclusively oxidize very-long chain fatty acids (>C20) (Cipolla and Lodhi, 2017). While mitochondria are believed to be the principal site of long chain fatty acid oxidation, peroxisomes also directly oxidize long chain fatty acids in a cooperative manner with mitochondria (Noland et al., 2007). The peroxisomal contribution to long chain fatty acid oxidation becomes quantitatively greater during physiologic states of increased fatty acid load such as fasting, diabetes, and high fat diets (Baes and Van

Veldhoven, 2016). The significant increase in linoleic and total fatty acids is consistent with an impairment in β-oxidation in fasted TMEM135 knockdown mice, and when considering hepatic NADH and ketone concentrations (Figure 5E-F), indicates that the impairment occurred in peroxisomes. Also, linoleic acid is an essential fatty acid obtained via dietary sources (Saini and Keum, 2018), which indicates that TMEM135 is not altering fatty acid synthesis or desaturation. With the exception of 22:6 that is derived from 18:3 (Saini and Keum, 2018), fasting itself did not increase any of the very-long chain fatty acids that are exclusively oxidized by peroxisomes and may explain why TMEM135 knockdown did not affect very-long chain fatty acid concentrations in fasted mice. Interestingly, in fed mice TMEM135 knockdown significantly decreased 22:0 and tended to decrease 24:0, indicating a slight increase in peroxisomal β-oxidation in the fed state. Regarding bile acids, hepatic concentrations of cholic acid were not significantly altered by TMEM135 knockdown (Figure S5). Collectively, these data indicate that TMEM135 may not be obligatory to basal peroxisome function, but under physiologic conditions of elevated hepatic fatty acid flux, TMEM135 may play a key role in enhancing peroxisomal function to assist the liver in meeting the increased demand for β-oxidation.

Discussion

Peroxisomes have key catabolic functions including α and β-oxidation of fatty acids, and anabolic activities including the synthesis of bile acids and ether phospholipids (Baes and Van Veldhoven, 2016; Waterham et al., 2016). There are 2 main classes of peroxisome disorders: 1) peroxisome biogenesis disorders, and 2) single peroxisomal enzyme deficiencies (Baes and Van Veldhoven, 2016; Waterham et al., 2016). Outcomes from these disorders range from infant death to mild degenerative neurosensory problems (Baes and Van Veldhoven, 2016; Waterham et al., 2016). Hepatic pathologies are one of the principal features associated with peroxisome disorders, which are often caused by a failure to import matrix enzymes into peroxisomes (Baes and Van Veldhoven, 2016). In the current study we determined that TMEM135 is an LXR-

inducible protein that regulates peroxisome function by mediating an auxiliary import pathway for matrix enzymes to enter peroxisomes.

Multiple lines of evidence support TMEM135 as being a regulator of peroxisome function. When hepatic β-oxidation (both peroxisomal and mitochondrial) was stimulated by fasting, TMEM135 knockdown mice had significantly lower NADH (Figure 5E) and significantly higher total fatty acid and linoleic acid concentrations (Figure 7C-D), indicating an impairment in β-oxidation. Meanwhile, hepatic ketones were significantly increased in knockdown mice when fasted (Figure 5F), and ketogenesis occurs exclusively in mitochondria and is intricately linked to β-oxidation (Newman and Verdin, 2017). Collectively, these findings indicate that β-oxidation was impaired in peroxisomes, but not in mitochondria. The increase in ketones may have resulted from the increased availability of fatty acids to the mitochondria and/or due to the increased NAD+/NADH ratio, both of which stimulate ketogenesis (Newman and Verdin, 2017). Additionally, many effects of hepatocyte-specific TMEM135 knockdown in the current study are consistent with typical features of peroxisome dysfunction. Liver-specific peroxisome deficiency in mice (peroxisomal biogenesis factor 5 or *Pex5* conditional knockout) results in hepatic fat accumulation despite significantly reduced mRNA expression of *Srebf1* and increased PPARA target gene mRNA expression, and a stunting of body growth (Peeters et al., 2011). In our study, knockdown of TMEM135 caused fatty acid accumulation both *in vitro* and *in vivo*. In HepG2 cells, increased triglycerides occurred despite a simultaneous significant reduction in mRNA expression of *SREBF1* (Figure 4A-B), and some PPARA target genes were increased by TMEM135 knockdown in fed mice (Figure 5D). Also, TMEM135 knockdown caused a significant reduction in body weight gain of knockdown mice in the fed state (Figure 5C). Collectively, these data indicate that TMEM135 mediates peroxisome function.

Mechanistically, our data indicate that TMEM135 modulates peroxisome function by regulating the import of matrix enzymes into peroxisomes. This differs from the classical mechanism involving peroxisomal targeting signals (PTS), which are short amino acid sequences

at the N or C-terminus that interact with various members of the peroxin family of proteins to facilitate import into the peroxisome matrix (Haimovich et al., 2016). Among the proteins whose import was quantified by Western blot in the current study ACOX1 and SCP2 contain a PTS1 sequence on their C-terminus that is recognized by PEX5, and ACAA1 contains a PTS2 sequence at its N-terminus that interacts with PEX7 (peroxisomal biogenesis factor 7) (Haimovich et al., 2016; Mizuno et al., 2013). Therefore, TMEM135 is likely not obligatory for their import, but rather serves an auxiliary role. It is not known whether TMEM135-mediated protein import occurs via a mechanism that involves, or occurs independently of, peroxins. Because TMEM135 is a transmembrane protein with TIM17 homology (Zarsky and Dolezal, 2016), a peroxin-independent mechanism seems most likely. Regardless, TMEM135-mediated protein import may be necessary under conditions of high peroxisome activity when peroxin-dependent import becomes saturated, which is consistent with our finding that fasting-induced hepatic β-oxidation is dependent on TMEM135.

An auxiliary role of TMEM135 in peroxisome protein import makes it a potential therapeutic target, and because it is also an LXR target gene in humans, pharmacologic modulation of the LXRs may be useful for altering peroxisome metabolism. The LXRs are master regulators of reverse cholesterol transport (RCT), a process whereby excess cholesterol is removed from peripheral tissues and transported to the liver for elimination in bile acids (Hong and Tontonoz, 2014). There has been much interest in the development of LXR agonists to treat human diseases including atherosclerosis, Alzheimer's disease, and other metabolic disorders (Hong and Tontonoz, 2014). However, the therapeutic potential of LXR agonists has been limited because they also increase hepatic lipogenesis via induction of SREBP1c (Repa et al., 2000; Yoshikawa et al., 2001). Our data indicate that the LXRs can stimulate peroxisomal β-oxidation by increasing transcription of *TMEM135*, which consequently may limit steatosis during LXR-induced lipogenesis. It should be noted that our data indicate that *TMEM135* is an LXR target gene in humans, but in mice *Tmem135* is either not induced by the LXRs or is a low-affinity target gene

(Figure S2). Thus, LXR agonist-induced steatosis may be less pronounced in human compared to mice hepatocytes due to species differences in LXR regulation of *TMEM135* transcription. Previous evidence of a link between the LXRs and peroxisomal β-oxidation is limited and conflicting. One group reported increased hepatic peroxisomal β-oxidation in mice treated with an LXR agonist through an undefined mechanism involving increased oxidative gene expression (Beyer et al., 2004; Hu et al., 2005). However, another report indicates that the LXRs suppress peroxisomal β-oxidation by inhibiting expression of the peroxisomal membrane transporter ABCD2 (Gondcaille et al., 2014). It would be interesting to determine how LXR-mediated suppression of ABCD2 and induction of TMEM135 influences overall peroxisome function.

Elevated TMEM135 may protect against lipid loading but may also contribute to hepatic pathologies. For example, metabolomics studies have reported that elevated serum bile acids and urinary bile salts represent the core metabolic phenotype in the transition from healthy liver to nonalcoholic fatty liver disease, nonalcoholic steatohepatitis, cirrhosis, and HCC (Beyoglu and Idle, 2013). Additionally, elevated β-oxidation and reduced mitochondrial respiration are part of the metabolic remodeling that occurs in chronic liver disease (Beyoglu and Idle, 2013). These metabolic changes are consistent with high peroxisome activity as peroxisomes play a key role in bile acid synthesis, they contribute to fatty acid β-oxidation, and can also indirectly alter mitochondrial respiration (Baes and Van Veldhoven, 2016). In the current study TMEM135 knockdown reduced proliferation of the HepG2 cell line by increasing G0/G1 arrest. Also, a metabolomics study found that linoleic acid is significantly reduced in human HCC tumors compared to nontumor liver tissue from the same subjects (Beyoglu et al., 2013), and in our data linoleic acid was significantly increased by TMEM135 knockdown *in vivo* (Figure 7C), consistent with a role for TMEM135 in pathogenic β-oxidation. There is additional evidence in the literature of an oncogenic role for TMEM135. It was among genes identified by transcriptomic analysis as being significantly reduced in expression when proliferation of HepG2 and Huh7 cells were inhibited by knockdown of the COP9 signalosome subunit 5 (Lee et al., 2011). Also, a genomic

rearrangement that results in a TMEM135-containing fusion transcript has been linked with aggressive prostate cancer (Yu et al., 2014), and Cas9-mediated insertion of a suicide gene into cells expressing this same fusion transcript reduces tumor burden and mortality in mouse xenografts (Chen et al., 2017). Thus, TMEM135 may represent a novel target in the treatment of certain cancers and chronic liver disease.

Previous studies to determine the biological function of TMEM135 are limited. The first indication of its function came from a mouse model of mitochondrial acyl-CoA dehydrogenase very long chain (ACADVL) deficiency (Exil et al., 2010). Under conditions of increased demand for β-oxidation such as fasting and cold stress, ACADVL-deficient mice have reduced survival due to cardiac dysfunction (Exil et al., 2010). It was discovered that TMEM135 was elevated more than four-fold in the hearts of ACADVL-deficient mice that survived birth (Exil et al., 2010). The ACADVL enzyme catalyzes the first step in mitochondrial β-oxidation using fatty acids larger than 14 carbons as substrates (McAndrew et al., 2008). Because ACADVL deficiency restricts the mitochondria from directly oxidizing long chain fatty acids, data from the current study indicate that the increase in TMEM135 likely promoted survival by increasing peroxisomal β-oxidation and the processing of long and very-long chain fatty acids to medium chain fatty acids that were subsequently oxidized in the mitochondria in an ACADVL-independent manner. Another study into TMEM135 function reported that a mutation in *Tmem135* was responsible for accelerated aging of the retina in a mouse model of age-related macular degeneration (Lee et al., 2016). Neurodegenerative disorders are commonly associated with peroxisome dysfunction (Cipolla and Lodhi, 2017), which is consistent with a *Tmem135* mutation causing accelerated aging in the retina. Both of these previous studies on TMEM135 reported that it is localized to mitochondria (Exil et al., 2010; Lee et al., 2016), whereas our data indicates it functions in peroxisomes. In support of a peroxisomal origin of action, another previous study clearly demonstrated that TMEM135 (formerly known as PMP52) is localized to peroxisomes and not mitochondria (Wiese et al., 2007). Because peroxisomes and mitochondria can physically associate via the formation

of tethering complexes (Schrader et al., 2015), it seems likely that reports of TMEM135 association with mitochondria (Exil et al., 2010; Lee et al., 2016) were due to peroxisomes that were tethered to mitochondria, and TMEM135 effects on mitochondria are indirectly mediated via altered peroxisome function.

The critical role of peroxisomes in human health is illustrated by the spectrum of peroxisome disorders; but in addition to these inborn errors of metabolism it is becoming increasingly apparent that peroxisomes play key roles in other metabolic and age-related diseases including cancer, neurodegenerative disorders, and diabetes (Cipolla and Lodhi, 2017). This may be due to direct catabolic and anabolic actions of peroxisomes, as well as interactions between peroxisomes and other organelles including mitochondria (Cipolla and Lodhi, 2017; Schrader et al., 2015). Our data indicate that TMEM135 regulates peroxisome function by mediating an auxiliary matrix protein import pathway. Furthermore, the effects of TMEM135 are inducible as it is an LXR target gene in humans, and it is likely to be regulated by other metabolic signaling pathways. In support of this, PPARA is the master regulator of β-oxidation in the liver and in primary human hepatocytes *TMEM135* mRNA expression is consistently induced by PPARA agonists (Kersten and Stienstra, 2017) and its promoter is bound by PPARA as determined using ChIP-seq (McMullen et al., 2014), indicating it is also a PPARA target gene. These findings implicate TMEM135 as a potential therapeutic target in the treatment of metabolic and age-related diseases that are associated with peroxisome dysfunction.

Acknowledgements

Mass spectrometry and proteomics data were acquired by the Arizona Proteomics Consortium at the BIO5 Institute of the University of Arizona. The authors would like to thank Dr. Jon Hennebold at the Oregon National Primate Research Center of Oregon Health & Science University for assistance with the unpublished microarray experiment in macaque luteal cells that provided preliminary data for the current study. The authors would also like to thank Dr. André-Denis Wright for arranging Departmental support to ensure completion of this project. This

research was supported by the Eunice Kennedy Shriver National Institute of Child Health & Human Development, National Institutes of Health, Award Number R00 HD067678 to R.L.B. The content is solely the responsibility of the authors and does not necessarily represent the official views of the National Institutes of Health. This work was also supported by the Arizona Biomedical Research Commission Early Stage Investigator Award No. ADHS14-082986 to B.J.R.

Author Contributions

Conceptualization, R.L.B. and B.J.R.; Methodology R.L.B. and B.J.R.; Investigation, R.L.B., B.J.R., T.W.M., S.G., C.E.G., and Y.X.; Resources, R.L.B. and B.J.R.; Writing – Original Draft, R.L.B.; Writing – Review & Editing, R.L.B. and B.J.R.; Funding Acquisition, R.L.B. and B.J.R.

Declaration of Interests

The authors declare no competing interests.

References

Baes, M., and Van Veldhoven, P.P. (2016). Hepatic dysfunction in peroxisomal disorders. Biochim Biophys Acta *1863*, 956-970.

Beyer, T.P., Schmidt, R.J., Foxworthy, P., Zhang, Y., Dai, J., Bensch, W.R., Kauffman, R.F., Gao, H., Ryan, T.P., Jiang, X.C., et al. (2004). Coadministration of a liver X receptor agonist and a peroxisome proliferator activator receptor-alpha agonist in Mice: effects of nuclear receptor interplay on high-density lipoprotein and triglyceride metabolism in vivo. J Pharmacol Exp Ther *309*, 861-868.

Beyoglu, D., and Idle, J.R. (2013). The metabolomic window into hepatobiliary disease. J Hepatol *59*, 842-858.

Beyoglu, D., Imbeaud, S., Maurhofer, O., Bioulac-Sage, P., Zucman-Rossi, J., Dufour, J.F., and Idle, J.R. (2013). Tissue metabolomics of hepatocellular carcinoma: tumor energy metabolism and the role of transcriptomic classification. Hepatology *58*, 229-238.

Cartharius, K., Frech, K., Grote, K., Klocke, B., Haltmeier, M., Klingenhoff, A., Frisch, M., Bayerlein, M., and Werner, T. (2005). MatInspector and beyond: promoter analysis based on transcription factor binding sites. Bioinformatics *21*, 2933-2942.

Chen, Z.H., Yu, Y.P., Zuo, Z.H., Nelson, J.B., Michalopoulos, G.K., Monga, S., Liu, S., Tseng, G., and Luo, J.H. (2017). Targeting genomic rearrangements in tumor cells through Cas9-mediated insertion of a suicide gene. Nat Biotechnol *35*, 543-550.

Cipolla, C.M., and Lodhi, I.J. (2017). Peroxisomal Dysfunction in Age-Related Diseases. Trends Endocrinol Metab *28*, 297-308.

Costet, P., Luo, Y., Wang, N., and Tall, A.R. (2000). Sterol-dependent transactivation of the ABC1 promoter by the liver X receptor/retinoid X receptor. J Biol Chem *275*, 28240-28245.

Exil, V.J., Silva Avila, D., Benedetto, A., Exil, E.A., Adams, M.R., Au, C., and Aschner, M. (2010). Stressed-induced TMEM135 protein is part of a conserved genetic network involved in fat storage and longevity regulation in Caenorhabditis elegans. PLoS One *5*, e14228.

Geisler, C.E., Hepler, C., Higgins, M.R., and Renquist, B.J. (2016). Hepatic adaptations to maintain metabolic homeostasis in response to fasting and refeeding in mice. Nutr Metab (Lond) *13*, 62.

Gondcaille, C., Genin, E.C., Lopez, T.E., Dias, A.M., Geillon, F., Andreoletti, P., Cherkaoui-Malki, M., Nury, T., Lizard, G., Weinhofer, I., et al. (2014). LXR antagonists induce ABCD2 expression. Biochim Biophys Acta *1841*, 259-266.

Haimovich, G., Cohen-Zontag, O., and Gerst, J.E. (2016). A role for mRNA trafficking and localized translation in peroxisome biogenesis and function? Biochim Biophys Acta *1863*, 911-921.

Harper, J.W., and Adams, P.D. (2001). Cyclin-dependent kinases. Chem Rev *101*, 2511-2526.

Hong, C., and Tontonoz, P. (2014). Liver X receptors in lipid metabolism: opportunities for drug discovery. Nat Rev Drug Discov *13*, 433-444.

Hu, T., Foxworthy, P., Siesky, A., Ficorilli, J.V., Gao, H., Li, S., Christe, M., Ryan, T., Cao, G., Eacho, P., et al. (2005). Hepatic peroxisomal fatty acid beta-oxidation is regulated by liver X receptor alpha. Endocrinology *146*, 5380-5387.

Jensen, J.T., Addis, I.B., Hennebold, J.D., and Bogan, R.L. (2017). Ovarian Lipid Metabolism Modulates Circulating Lipids in Premenopausal Women. J Clin Endocrinol Metab *102*, 3138-3145.

Kennedy, M.A., Venkateswaran, A., Tarr, P.T., Xenarios, I., Kudoh, J., Shimizu, N., and Edwards, P.A. (2001). Characterization of the human ABCG1 gene: liver X receptor activates an internal promoter that produces a novel transcript encoding an alternative form of the protein. J Biol Chem *276*, 39438-39447.

Kersten, S., and Stienstra, R. (2017). The role and regulation of the peroxisome proliferator activated receptor alpha in human liver. Biochimie *136*, 75-84.

Laffitte, B.A., Joseph, S.B., Walczak, R., Pei, L., Wilpitz, D.C., Collins, J.L., and Tontonoz, P. (2001). Autoregulation of the human liver X receptor alpha promoter. Mol Cell Biol *21*, 7558-7568.

LaPak, K.M., and Burd, C.E. (2014). The molecular balancing act of p16(INK4a) in cancer and aging. Mol Cancer Res *12*, 167-183.

Lee, W.H., Higuchi, H., Ikeda, S., Macke, E.L., Takimoto, T., Pattnaik, B.R., Liu, C., Chu, L.F., Siepka, S.M., Krentz, K.J., et al. (2016). Mouse Tmem135 mutation reveals a mechanism involving mitochondrial dynamics that leads to age-dependent retinal pathologies. Elife *5*.

Lee, Y.H., Judge, A.D., Seo, D., Kitade, M., Gomez-Quiroz, L.E., Ishikawa, T., Andersen, J.B., Kim, B.K., Marquardt, J.U., Raggi, C., et al. (2011). Molecular targeting of CSN5 in human hepatocellular carcinoma: a mechanism of therapeutic response. Oncogene *30*, 4175-4184.

Masood, A., Stark, K.D., and Salem, N., Jr. (2005). A simplified and efficient method for the analysis of fatty acid methyl esters suitable for large clinical studies. J Lipid Res *46*, 2299-2305.

McAndrew, R.P., Wang, Y., Mohsen, A.W., He, M., Vockley, J., and Kim, J.J. (2008). Structural basis for substrate fatty acyl chain specificity: crystal structure of human very-long-chain acyl-CoA dehydrogenase. J Biol Chem *283*, 9435-9443.

McMullen, P.D., Bhattacharya, S., Woods, C.G., Sun, B., Yarborough, K., Ross, S.M., Miller, M.E., McBride, M.T., LeCluyse, E.L., Clewell, R.A., et al. (2014). A map of the PPARalpha transcription regulatory network for primary human hepatocytes. Chem Biol Interact *209*, 14-24.

Mizuno, Y., Ninomiya, Y., Nakachi, Y., Iseki, M., Iwasa, H., Akita, M., Tsukui, T., Shimozawa, N., Ito, C., Toshimori, K., et al. (2013). Tysnd1 deficiency in mice interferes with the peroxisomal localization of PTS2 enzymes, causing lipid metabolic abnormalities and male infertility. PLoS Genet *9*, e1003286.

Newman, J.C., and Verdin, E. (2017). beta-Hydroxybutyrate: A Signaling Metabolite. Annu Rev Nutr *37*, 51-76.

Noland, R.C., Woodlief, T.L., Whitfield, B.R., Manning, S.M., Evans, J.R., Dudek, R.W., Lust, R.M., and Cortright, R.N. (2007). Peroxisomal-mitochondrial oxidation in a rodent model of obesity-associated insulin resistance. Am J Physiol Endocrinol Metab *293*, E986-E1001.

Peet, D.J., Janowski, B.A., and Mangelsdorf, D.J. (1998). The LXRs: a new class of oxysterol receptors. Curr Opin Genet Dev *8*, 571-575.

Peeters, A., Swinnen, J.V., Van Veldhoven, P.P., and Baes, M. (2011). Hepatosteatosis in peroxisome deficient liver despite increased beta-oxidation capacity and impaired lipogenesis. Biochimie *93*, 1828-1838.

Repa, J.J., Liang, G., Ou, J., Bashmakov, Y., Lobaccaro, J.M., Shimomura, I., Shan, B., Brown, M.S., Goldstein, J.L., and Mangelsdorf, D.J. (2000). Regulation of mouse sterol regulatory element-binding protein-1c gene (SREBP-1c) by oxysterol receptors, LXRalpha and LXRbeta. Genes Dev *14*, 2819-2830.

Saini, R.K., and Keum, Y.S. (2018). Omega-3 and omega-6 polyunsaturated fatty acids: Dietary sources, metabolism, and significance - A review. Life Sci *203*, 255-267.

Salway, J.G. (1969). The simultaneous determination of acetoacetate and glucose in capillary blood. Clin Chim Acta *25*, 109-116.

Schrader, M., Godinho, L.F., Costello, J.L., and Islinger, M. (2015). The different facets of organelle interplay-an overview of organelle interactions. Front Cell Dev Biol *3*, 56.

Schwartz, D.M., and Wolins, N.E. (2007). A simple and rapid method to assay triacylglycerol in cells and tissues. J Lipid Res *48*, 2514-2520.

Seto, N.L., and Bogan, R.L. (2015). Decreased cholesterol uptake and increased liver x receptor-mediated cholesterol efflux pathways during prostaglandin F2 alpha-induced and spontaneous luteolysis in sheep. Biol Reprod *92*, 128.

Stolowich, N.J., Petrescu, A.D., Huang, H., Martin, G.G., Scott, A.I., and Schroeder, F. (2002). Sterol carrier protein-2: structure reveals function. Cell Mol Life Sci *59*, 193-212.

Teboul, M., Enmark, E., Li, Q., Wikstrom, A.C., Pelto-Huikko, M., and Gustafsson, J.A. (1995). OR-1, a member of the nuclear receptor superfamily that interacts with the 9-cis-retinoic acid receptor. Proc Natl Acad Sci U S A *92*, 2096-2100.

Walker, P.G. (1954). A colorimetric method for the estimation of acetoacetate. Biochem J *58*, 699-704.

Waterham, H.R., Ferdinandusse, S., and Wanders, R.J. (2016). Human disorders of peroxisome metabolism and biogenesis. Biochim Biophys Acta *1863*, 922-933.

Whitney, K.D., Watson, M.A., Goodwin, B., Galardi, C.M., Maglich, J.M., Wilson, J.G., Willson, T.M., Collins, J.L., and Kliewer, S.A. (2001). Liver X receptor (LXR) regulation of the LXRalpha gene in human macrophages. J Biol Chem *276*, 43509-43515.

Wiese, S., Gronemeyer, T., Ofman, R., Kunze, M., Grou, C.P., Almeida, J.A., Eisenacher, M., Stephan, C., Hayen, H., Schollenberger, L., et al. (2007). Proteomics characterization of mouse kidney peroxisomes by tandem mass spectrometry and protein correlation profiling. Mol Cell Proteomics *6*, 2045-2057.

Willy, P.J., Umesono, K., Ong, E.S., Evans, R.M., Heyman, R.A., and Mangelsdorf, D.J. (1995). LXR, a nuclear receptor that defines a distinct retinoid response pathway. Genes Dev *9*, 1033-1045.

Xu, Y., Hernandez-Ledezma, J.J., Hutchison, S.M., and Bogan, R.L. (2018a). The liver X receptors and sterol regulatory element binding proteins alter progesterone secretion and are regulated by human chorionic gonadotropin in human luteinized granulosa cells. Mol Cell Endocrinol *473*, 124-135.

Xu, Y., Hutchison, S.M., Hernandez-Ledezma, J.J., and Bogan, R.L. (2018b). Increased 27-hydroxycholesterol production during luteolysis may mediate the progressive decline in progesterone secretion. Mol Hum Reprod *24*, 2-13.

Yoshikawa, T., Shimano, H., Amemiya-Kudo, M., Yahagi, N., Hasty, A.H., Matsuzaka, T., Okazaki, H., Tamura, Y., Iizuka, Y., Ohashi, K., et al. (2001). Identification of liver X receptor-retinoid X receptor as an activator of the sterol regulatory element-binding protein 1c gene promoter. Mol Cell Biol *21*, 2991-3000.

Yu, Y.P., Ding, Y., Chen, Z., Liu, S., Michalopoulos, A., Chen, R., Gulzar, Z.G., Yang, B., Cieply, K.M., Luvison, A., et al. (2014). Novel fusion transcripts associate with progressive prostate cancer. Am J Pathol *184*, 2840-2849.

Zarsky, V., and Dolezal, P. (2016). Evolution of the Tim17 protein family. Biol Direct *11*, 54.

Zelcer, N., Hong, C., Boyadjian, R., and Tontonoz, P. (2009). LXR regulates cholesterol uptake through Idol-dependent ubiquitination of the LDL receptor. Science *325*, 100-104.

Figure Legends

Figure 1: A synthetic LXR agonist induces TMEM135 expression in human hepatocyte (HepG2, Hep3B) and monocyte-derived macrophage (THP-1) cell lines via a direct transcriptional mechanism. Panel A contains the results from treatment of HepG2 cells in the presence or absence of the synthetic LXR agonist T09 for 6, 12, 24 and 48 hours; while panel B is the effect of a 24-hour T09 treatment on *TMEM135* mRNA expression in Hep3B cells (n = 4). Panel C is a time course of T09 treatment in THP-1 cells (n = 4). For panels A-C, asterisks denote significant ($p < 0.05$) difference between DMSO and T09 at the indicated timepoint. Panel D is the effect of the protein synthesis inhibitor cycloheximide on *TMEM135* mRNA expression in THP-1 cells. Cells were treated for 24 hours in a 2 × 2 factorial with T09 and cycloheximide (n = 5). Columns with different letters are significantly different ($p < 0.05$). Panel E is Western blot analysis of TMEM135 protein in the mitochondria/peroxisome-enriched fraction of HepG2 cells treated with or without T09 for 24 hours (n = 4). The approximate molecular weights of the protein ladder are indicated, as well as the TMEM135 and COX4I1 (housekeeping control) bands. Panel F is results of densitometry analysis of the blot shown in Panel E, asterisk denotes significant difference ($p < 0.05$). For all panels, error bars indicate ± one standard error of the mean (SEM).

Figure 2: The LXRs bind all three potential LXREs in the human *TMEM135* promoter with LXRE3 mediating LXR-induced *TMEM135* transcription. Panel A is an EMSA using LXRE1 as the fluorescent probe. The nuclear receptor(s) used in the reaction are indicated beneath the

image, with the unlabeled competitor DNA (200-fold molar excess) shown above the image. Panel B substitutes NR1H2 for NR1H3 in the binding reactions. Panel C utilizes fluorescent LXRE3 as the probe. The image has been cropped to only show the bound and free fluorescent LXRE3 probe. The nuclear receptor(s) used in the reaction are indicated beneath the image. Increasing amounts (0.25, 0.5, 1, 2, and 10-fold molar excess per competitor) of unlabeled LXRE1 or LXRE3 were included in some reactions as indicated above the images. In Panel D, an EMSA was performed using a mixture of LXRE1 and LXRE3 probes that were labeled with spectrally-distinct fluorescent dyes, as well as increasing quantities of LXR/RXR proteins. The percent of each probe bound in each reaction was determined by densitometry and plotted. Panel E displays luciferase activity (arbitrary units normalized to β-galactosidase) derived from cells transfected with the empty vector or the *TMEM135* promoter-containing construct in the presence and absence of T09. The effect of increased expression of NR1H3 and RXRA is also shown (n = 4). Panel F contains the fold-increase in luciferase activity induced by T09 from the wild type *TMEM135* promoter, as well as *TMEM135* promoters containing all possible combinations of mutant LXRE sites (n = 4). All transfections in Panel F included *NR1H3* and *RXRA* co-transfection to increase basal expression of these nuclear receptors. An X indicates point mutations were introduced into the corresponding LXRE (see Figure S1), Luc = luciferase. Error bars indicate one SEM, columns without common letters are significantly ($p < 0.05$) different. See also Figures S1 and S2.

Figure 3: The LXRs are obligatory for LXR agonist-induced *TMEM135* mRNA expression, and cause transcription of *TMEM135* with an abbreviated 5' UTR. Panels A, B, C, and D show the effects of siRNA transfection in HepG2 cells on T09-induced mRNA expression of the LXR isoforms *NR1H2* and *NR1H3*, *ABCA1*, and *TMEM135*; respectively. Panel E shows the effect of LXR knockdown in HepG2 cells on T09-induced expression of *TMEM135* mRNA transcripts containing the full 5' UTR. Primers and probe used for QPCR in panel E amplify a 76 bp region within the 5' UTR that encompasses the LXR binding site in genomic DNA. Panel F is results from

ChIP analysis. For all panels, error bars indicate one SEM, columns without common letters are significantly ($p < 0.05$) different ($n = 4$).

Figure 4: TMEM135 regulates fatty acid metabolism and proliferation of HepG2 cells. Panel A displays the effect of TMEM135 knockdown in the presence and absence of the lipogenic LXR agonist T09 on intracellular triglyceride accumulation in HepG2 cells. Panel B is mRNA expression in HepG2 cells for *TMEM135*, genes involved in fatty acid oxidation (*PPARA*, *CPT1A*), and genes involved in fatty acid synthesis (*SREBF1*, *FASN*). For panels A and B, columns without a common letter are significantly ($p < 0.05$) different ($n = 4$). Panel C is the effect of TMEM135 knockdown on ATP content (normalized to total protein content) in HepG2 cells after a 4-hour incubation in glucose-free, sodium pyruvate-free media. The chart is plotted with the control siRNA set to 1, and the asterisk denotes a significant difference ($n = 4$). Panel D is the effect of TMEM135 knockdown on proliferation of HepG2 cells. Asterisks denote significant difference at the corresponding timepoint ($n = 4$). Panel E is the effect of TMEM135 knockdown on cell cycle progression in HepG2 cells, and panel F is the effect on mRNA expression of cell cycle-associated genes. For panels E-F, asterisks denote significant differences due to TMEM135 knockdown ($n = 4$).

Figure 5: Liver-specific knockdown of TMEM135 inhibits peroxisomal β-oxidation. Panel A is mRNA expression of *Tmem135* in the listed tissues isolated from fed mice ($n = 5$). Panel B displays TMEM135 protein expression in the mitochondria/peroxisome-enriched fraction from livers. The right half of the image was incubated with antibody pre-absorbed with the immunizing peptide. The sample contained in each lane is indicated beneath the images: MW = molecular weight marker, Con = control siRNA, KD = Knockdown, *Tmem135* siRNA. The chart in panel B displays the results of densitometry analysis of all 3 TMEM135 bands in the mitochondria/peroxisome-enriched fraction of mice liver (fed and fasted animals pooled, $n = 10$ mice), as well as spectral counts from one peptide identified via proteomic analysis that was mapped to TMEM135 ($n = 3$, fed animals only). In Panels A-B, asterisks denote significant

difference due to *Tmem135* siRNA. Panel C displays the change in body weight of animals from the time of siRNA injection until sacrifice 4 days later (n = 5). Panel D displays hepatic mRNA expression of *Tmem135* and genes involved in fatty acid oxidation, panel E displays hepatic NAD concentrations, and Panel F is hepatic ketone concentrations (total ketones = β-hydroxybutyrate + acetoacetate). For panels C-F, asterisks denote significant difference ($p < 0.05$) due to *Tmem135* siRNA within feeding status, and # indicates significant difference due to fasting in animals receiving control siRNA (n = 5). See also Figures S3 and S4.

Figure 6: TMEM135 mediates import of peroxisome matrix enzymes. Panel A displays the relative purity of the mitochondria/peroxisome-enriched fraction used for proteomic analysis as determined by Western blot analysis of controls for mitochondria (COX4I1), peroxisome (ABCD3), and cytosolic (TUBB) proteins. For each image, the lanes from left to right are the molecular weight marker (MW), whole cell lysate (WC), cytosolic fraction (Cyto), and the mitochondria/peroxisome-enriched fraction (M/P). Panel B are proteins significantly decreased (Fisher's Exact Test, $p < 0.05$) in the mitochondria/peroxisome-enriched fraction from TMEM135 knockdown livers, as well as the respective mean ± SEM of their spectral counts (n = 3, fed mice only). Panel C illustrates peroxisomal β-oxidation of very-long chain fatty acids (VLCFA) and dicarboxylic acids (DCA). VLCFA and DCA are transported into peroxisomes via ABCDs (ABCD members 1-3). Panel D illustrates peroxisomal bile acid synthesis and β-oxidation of branched chain fatty acids (BCFA). Bile acid intermediates (BAI) and BCFA are transported into peroxisomes via the ABCD proteins. CA = cholic acid, CDCA = chenodeoxycholic acid, BrAcyl-CoA = branched chain acyl-CoA. For panels C-D, the enzymes catalyzing each step are shown in boxes, and enzymes that were significantly less abundant in the mitochondria/peroxisome-enriched fraction from TMEM135 knockdown mice (Panel B) are shaded. Panel E displays relative peroxisome content in the mitochondria/peroxisome-enriched fractions as determined by proteomic and Western blot analysis. For proteomics, only fed mice were analyzed (n = 3). For Western blot, the ABCD3:COX4I1 ratio in the mitochondria/peroxisome-enriched fraction is

shown (n = 5). Panel F is subcellular distribution of ACAA1, ACOX1, SCP2, and CAT. ACOX1 migrates in 2 separate bands in Western blot, with the smaller band being proteolytically processed ACOX1 (Mizuno et al., 2013). Furthermore, SCP2 (also known as SCPx) is a 58 kDa protein that contains a 45 kDa 3-ketoacyl CoA thiolase domain and a 13 kDa sterol-carrier domain (Stolowich et al., 2002), which are separated by proteolytic cleavage (Mizuno et al., 2013). The antibody used in the current study recognizes the full-length 58 kDa protein (indicated by arrow) and the 45 kDa 3-ketoacyl CoA thiolase domain, but not the 13 kDa sterol-carrier domain. The identity of the other bands in the SCP2 blot is not known.

Figure 7: Reduced peroxisomal import of matrix enzymes impairs β-oxidation. Panel A contains images from Western blot analysis of whole cell and mitochondria/peroxisome-enriched fractions (Mito/Perox-Enriched Fraction) in livers of fed and fasted mice. Loading controls were TUBB for whole cell lysates, COX4I1 for mitochondria, and ABCD3 for peroxisomes. The siRNA treatment is indicated beneath the lanes, Con = control siRNA, KD = Knockdown, *Tmem135* siRNA. For SCP2, the band used for densitometry analysis is indicated by asterisks. Panel B displays the results of densitometry analysis of the blots shown in Panel A. Peroxisome import was determined by first normalizing each protein in the mitochondria/peroxisome-enriched fraction to ABCD3 to account for differences in peroxisome content, and the ratio relative to the whole cell lysate (normalized to TUBB) was used to determine peroxisome import. Panel C plots concentrations of C18 fatty acids quantified by GC. In panels B-C, asterisks denote significant difference ($p < 0.05$) within feeding status due to *Tmem135* siRNA, and # indicates significant difference due to fasting in mice receiving the control siRNA (n = 5). Panel D displays the mean ± SEM for all fatty acids (µg fatty acid per mg protein) quantified by GC. In the P column, asterisks denote significant difference ($p < 0.05$) and ^ denotes trends ($0.05 < p < 0.1$) within feeding status due to *Tmem135* siRNA. In the fasted mice control siRNA column, # indicates significant ($p < 0.05$) difference due to fasting in control siRNA mice. See also Figure S5.

STAR Methods

CONTACT FOR REAGENT AND RESOURCE SHARING

Further information and requests for resources and reagents should be directed to and will be fulfilled by the Lead Contact, Randy L. Bogan (boganr@email.arizona.edu). Transfer of resources is subject to the acceptance of a Material Transfer Agreement as required by policy at the University of Arizona. Resources are transferred and distributed by several means according to the needs of the end-user. For other academic and non-profit researchers, the resources are typically transferred under standard Material Transfer Agreements. For requests by for-profit organizations, the resources are made available under standard non-exclusive license.

EXPERIMENTAL MODEL AND SUBJECT DETAILS

Cell Lines

All cell lines were obtained from American Type Culture Collection (ATCC) and were cultured at 37°C, 5% CO_2 in air, in a humidified incubator. Human cells (all derived from males) included the hepatocyte lines HepG2 (ATCC® HB-8065™) and Hep 3B2.1-7 [Hep3B] (ATCC® HB-8064™), and the monocyte line THP-1 (ATCC® TIB-202™). Murine cells included the hepatocyte line (embryonic-derived) BNL 1NG A.2 (ATCC® TIB-76™) and the macrophage line (male) RAW 264.7 (ATCC® TIB-71™). Growth media for all cell lines except THP-1 was DMEM/F12 (Sigma Aldrich, Inc.) supplemented with Pen/Strep (100 units/ml penicillin and 100 µg/ml streptomycin) and 10% fetal bovine serum (FBS). THP-1 cells were incubated in RPMI media (Sigma) supplemented with 2-mercaptoethanol (0.05 mM), Pen/Strep, and 10% FBS. THP-1 cells were differentiated into macrophages by treatment with 12-myristate-13-acetate (PMA, 100 ng/ml) for 5 days prior to experimentation.

Mice

All procedures involving mice were approved by the University of Arizona IACUC. Male C57BL/6 mice, 12 weeks of age, were used. Mice were group housed until initiation of experimental procedures, at which point they were switched to individual caging.

METHOD DETAILS

Cell Treatments

T0901317 (Cayman Chemical, Inc.) was dissolved in DMSO and used at a 1 µM concentration unless indicated otherwise. Cycloheximide (ACROS Organics, Inc.) was dissolved in DMSO and used at a final concentration of 50 µg/ml. The final DMSO concentration was held constant in all groups at less than 0.2% (*v:v*). For siRNA knockdown experiments, Silencer® select pre-designed siRNAs (Life Technologies, Inc.) against human *NR1H2* (s14684), *NR1H3* (s19568), *TMEM135* (s35201), and a negative control siRNA (catalog 4390843) were purchased and transfected into HepG2 cells using Lipofectamine® RNAiMAX (Life Technologies) or TransIT-siQuest® reagent (Mirus Bio, LLC.) according to manufacturer instructions. All experiments were repeated 4-5 times on different days or with different passages of cells.

HepG2 Mitochondria/Peroxisome-Enriched Fraction Isolation

Cells were harvested and washed three times in 1 ml cell resuspension buffer (1 mM Tris-HCl, pH 7.4, 130 mM NaCl, 5 mM KCl, 7.5 mM $MgCl_2$). Cells were then resuspended in 600 µl homogenization buffer (10 mM Tris-HCl, pH 7.4, 10 mM KCl, 0.15 mM $MgCl_2$, plus protease and phosphatase inhibitor cocktail), incubated on ice for 10 min, and homogenized for 30 strokes in a glass dounce homogenizer with a tight-fitting pestle. The homogenate was mixed with 100 µl of 2M sucrose and centrifuged at 1,200 × g for 5 min at 4° C, and the supernatant transferred to a new tube. This low speed centrifugation step was repeated two more times. Mitochondria and peroxisomes were pelleted by centrifugation at 7,000 × g for 10 min at 4° C and the supernatant removed. The pellet was washed once with 300 µl of wash buffer (10 mM Tris-HCl, pH 7.4, 0.15 mM $MgCl_2$, 250 mM sucrose), and centrifuged at 9,500 × g for 5 min. Pellets were solubilized in RIPA buffer containing protease and phosphatase inhibitors, and protein concentration was determined by BCA assay (Fisher Scientific) following manufacturer recommendations.

Electrophoretic Mobility-Shift Analysis (EMSA)

The DNA sequences for human *NR1H2*, *NR1H3*, and RXR α (*RXRA*) were synthesized by Life Technologies and cloned into the pTarget™ mammalian expression vector (Promega

786 Corporation) using XhoI and KpnI restriction enzyme sites. Inserts were confirmed by DNA
787 sequence analysis. Recombinant NR1H2, NR1H3, and RXRA proteins were produced using the
788 TNT® Quick Coupled Transcription/Translation System (Promega). Fluorescent probes were
789 synthesized by Integrated DNA Technologies and corresponded to the LXRE1 sequence with
790 IRDye 700 attached to the 5' end, and probes corresponding to the LXRE3 sequence were
791 labelled with IRDye 800. Additionally, unlabeled DNA oligos corresponding to LXREs 1-3, as well
792 as mutated LXREs 1-3, were synthesized (Figure S1B). Single stranded DNA oligos were
793 annealed by mixing sense and antisense oligos in a 1:1 molar ratio, heating to 100°C for 5
794 minutes, and slowly cooling to room temperature. The EMSA binding reactions were carried out
795 for 30 min at room temperature in 10 mM Tris, 50 mM KCl, pH 7.5; 3.5 mM DTT, 0.25% Tween-
796 20, 1 µg Poly (dI.dC), 5 nM fluorescent probe (1 nM each for LXRE1/LXRE3 competition
797 experiment), and 1.5 µl of TNT lysate per protein (non-induced TNT lysate substituted in control
798 reactions). Unlabeled competitor DNA was added prior to the addition of fluorescent probe at a
799 200-fold molar excess unless indicated otherwise. Following the incubation period, EMSA
800 reactions were resolved on a 6% TBE gel (Life Technologies). Imaging and densitometry were
801 performed with a Li-COR Odyssey CLx and Image Studio version 3.1 software, respectively.

802 Reporter Assays

803 The region from -2662 to -1 bp (relative to translation start site) of the human *TMEM135*
804 promoter was synthesized by Life Technologies. Additionally, the same region of the human
805 *TMEM135* promoter was synthesized except that point mutations were introduced into each of
806 the three LXREs (Figure S1B). The normal and mutant *TMEM135* promoters were cloned into the
807 pGL4.17 vector (Promega) using SacI and XhoI restriction enzyme sites, which expresses firefly
808 luciferase from a promoter cloned into the vector. A unique PacI site was identified in the region
809 between LXRE1 and LXRE2, and a unique EcoRI site was identified in the region between LXRE2
810 and LXRE3. These restriction sites were used to generate six more *TMEM135* promoter/pGL4.17
811 constructs so that all possible combinations of wild type and mutated LXREs were obtained. All

constructs were verified using DNA sequence analysis. These reporter vectors were transfected into HepG2 cells along with a β-galactosidase control plasmid (Promega) to normalize transfection efficiency. In some transfections, *NR1H3*/pTarget and *RXRA*/pTarget constructs were co-transfected. Vectors were transfected in a ratio of 60:20:10:10 (luciferase:β-galactosidase:NR1H3:RXRA) using Lipofectamine® 3000 according to manufacturer recommendations, with no-insert plasmids substituted in control transfections to keep DNA concentrations constant. Each vector combination was transfected in triplicate to HepG2 cells in 96 well plates, and cells were incubated with DNA/Lipofectamine complexes for 24 hours at which point media were changed and cells were treated for an additional 48 hours with DMSO or T09. Cell lysates were prepared using mammalian protein extraction reagent (Fisher), and the lysate was fractionated to quantify luciferase and β-galactosidase activity using luminescent detection kits (Fisher). The ratio of luciferase to β-galactosidase activity was calculated, and the fold-change in T09 vs DMSO treated cells was determined for each transfection.

Chromatin Immunoprecipitation (ChIP) Analysis

HepG2 cells were fixed for 10 min at room temperature with 1% formaldehyde. The reaction was quenched by adding glycine to a 125 mM final concentration and incubating 5 min at room temperature. The cells were trypsinized, harvested, and washed twice with PBS. Nuclei were isolated by incubating cell pellets in 500 µl of a hypotonic buffer for 15 min on ice (20 mM Tris-HCL, pH 7.4, 10 mM NaCl, 3 mM $MgCL_2$, with protease and phosphatase inhibitor cocktail from Promega). Triton X-100 detergent was added to a 0.5% *v:v* final concentration to lyse the cells followed by centrifugation at 1200 × g for 10 min to pellet nuclei. The supernatant was removed, and the nuclei pellet washed once with 500 µl hypotonic buffer. The pellet was resuspended in 500 µl of RIPA buffer with protease and phosphatase inhibitors, and nuclei were sonicated in an ice-water bath using a Branson 250 digital sonifier programmed to cycle at a 10% amplitude with 5 seconds on followed by 20 seconds off, and a 3-minute total sonication time that was determined in preliminary time-course studies to produce chromatin of optimal length

(approximately 200-1000 base pairs). The sonicated lysates were centrifuged at 8,000 × g for 1 minute and the supernatant recovered. An aliquot of cleared lysate was treated with 25 µg RNAse A and 50 µg proteinase K in a buffer containing 500 mM NaCl and heated at 65°C for 1.5 hours to reverse cross-links. The DNA concentration in this aliquot was determined using a fluorometric assay (Life Technologies) following manufacturer recommendations. The quantity of DNA used in each ChIP was held constant within replicates (8 to 10 µg), and 10% of the input amount was saved. Chromatin was diluted to a 500 µl final volume in binding/wash buffer (50 mM Tris, 150 mM NaCl, 1% Triton X-100) containing protease and phosphatase inhibitors, and 3 µg of antibody was added per reaction. Tubes were incubated on an end-over-end rotator at 4°C overnight. Antibodies used for ChIP were mouse monoclonal IgG2a including: 1) anti-NR1H3 (clone PPZ0412, R&D Systems catalog PP-PPZ0412-00), 2) anti NR1H2 (clone K8917, R&D Systems catalog PP-K8917-00), and 3) non-specific control IgG2a (clone MOPC-173, Abcam catalog ab18413). The following day 25 µl of Protein G-conjugated Dynabeads (Life Technologies) were added and incubated for 1 hour at 4°C. The beads were recovered using a magnet and washed three times at 4°C for 5 minutes each wash with 1 ml of binding/wash buffer. The beads were then washed once in final wash buffer (50mM Tris, 500 mM NaCl, 1% Triton X-100). Elutions were performed with 130 µl elution buffer (100mM $NaHCO_3$, 500mM NaCl, 1% SDS) containing 25 µg RNAse A and 50 µg proteinase K, and ChIP reactions and input controls were incubated on a thermal mixer at 65°C for 1.5 hours. The supernatant was recovered, and DNA purified using PCR purification columns (Life Technologies) following manufacturer recommendations. Purified DNA was analyzed by QPCR in a duplex reaction with primers and a Taqman probe specific for the region spanning LXRE3 on the *TMEM135* gene, and a non-specific locus was simultaneously quantified in the same reaction as a control for non-specific DNA carryover (Table S1). Serial dilutions of purified sonicated DNA were included to verify linear amplification and PCR efficiency, and Ct values from ChIP reactions and input controls were used to calculate the percentage of

DNA recovered relative to the input. Data were normalized by calculating the ratio of the TMEM135 LXRE3 to the non-specific chromatin locus.

Semi-Quantitative Real-Time PCR

Cells or tissue were homogenized in Trizol reagent for isolation of mRNA and were further purified over RNeasy columns according to manufacturer recommendations (Life Technologies). Concentrations of RNA were quantified by spectrophotometry, and 0.2-1 µg RNA was treated with DNAse I and reverse transcribed into cDNA using the High Capacity cDNA Reverse Transcription Kit (Life Technologies). Following reverse transcription, cDNA were diluted to 10 ng/µl (based on original RNA concentration) and used for semi-quantitative real-time PCR analysis (QPCR). Primer and probe sequences used for QPCR are listed in Table S1. The QPCR assays were performed on a StepOne Plus Real-Time PCR system (Life Technologies) using TaqMan® MGB probe or SYBR green detection. Relative mRNA abundance was determined by extrapolation of threshold (Ct) values from a standard curve of serial cDNA dilutions and normalized to the housekeeping gene mitochondrial ribosomal protein S10 (*MRPS10*).

Cell Proliferation Assay

HepG2 cells were plated at 15,000 cells per well in 96-well plates and transfected with siRNAs immediately. At the appropriate post-transfection time, viable cells were quantified using a CyQuant® Direct Cell Proliferation assay (Life Technologies) according to manufacturer recommendations, and fluorescence (excitation 495 nm, emission 527 nm) determined using a Synergy H1 plate reader (BioTek Instruments, Inc.) in area scanning mode to account for uneven cell distribution. The number of cells per well was estimated by extrapolation from a standard curve of increasing cell numbers that was generated at the time of plating.

Flow Cytometry Analysis of Cell Cycle

Freshly harvested HepG2 cell pellets were fixed by slow addition of 1 ml ice-cold 70% ethanol while vortexing and incubated at -20°C overnight. Fixed cells were harvested by centrifugation at 850 × g for 5 min and resuspended in 1 ml DNA staining buffer (100 µg/ml RNAse

A, 50 µg/ml propidium iodide, in PBS). Cells were incubated for 30 min at 37°C, placed on ice, and analyzed within one hour. A Becton Dickinson FACSCANTO II flow cytometer equipped with a 488 nm argon ion laser and a 585/42 bandpass filter was used for detection of bound propidium iodide. List mode data files consisting of 10,000 events were acquired and the percentage of cells in G0/G1, S, and G2/M stages was determined with CellQuest PRO software (BD Biosciences).

HepG2 ATP Quantification

At 48 hours post-siRNA transfection, HepG2 cells were switched to serum-free, glucose-free, sodium pyruvate-free DMEM media and incubated at 37°C for 4 hours. Cellular ATP concentrations were determined using a homogenous luminescent ATP detection kit (Abcam catalog ab113849). Additional HepG2 cells treated in parallel to those used for ATP determination were lysed in RIPA buffer and a BCA protein assay (Fisher) was performed, and ATP content was normalized to protein concentrations.

Triglyceride Quantification

HepG2 cells or frozen mouse liver were sonicated in PBS containing protease and phosphatase inhibitors (Promega) in an ice-water bath using a Branson 250 digital sonifier programmed to cycle at a 10% amplitude with 5 seconds on followed by 20 seconds off, and a 30 second total sonication time. Triglycerides were extracted using an organic solvent procedure optimized for triglycerides (Schwartz and Wolins, 2007). Lysates were diluted 1:1 with deionized water, and 400 µl of diluted lysate was combined in a glass tube with 1.8 ml of a 4:1 isopropanol:hexane mixture. Samples were vortexed for 1 minute and incubated at room temperature for 30 min. Next, 500 µl of a 1:1 hexane:diethyl ether solution was added, the samples were vortexed as before, and incubated at room temperature for 1 minute. One ml of deionized water was added, samples were vortexed as before, and incubated at room temperature for 20 minutes to allow phase separation. The organic phase was transferred to a new glass tube and dried under a gentle stream of nitrogen in a water bath at 30°C. Dried extracts were dissolved in 200 µl assay buffer (50 mM potassium phosphate, pH 7.0, 0.01% Triton X-100)

by 5 total cycles of vortexing for 1 minute and incubating at room temperature for 3 minutes. Extracts (50 µl/well) were transferred to a clear 96 well plate, and 250 µl of triglyceride detection reagent (Pointe Scientific, Inc., catalog T7532) was added. Triglyceride standards (Pointe Scientific) diluted in assay buffer were also run with each assay. Plates were incubated at 37°C for 30 minutes with vigorous shaking, and absorbance at 500 nm was determined with a Synergy H1 plate reader. The protein concentration in sonicated lysates was determined using a BCA protein assay, and triglyceride content was normalized to protein content.

In Vivo siRNA Delivery and Tissue Harvest

Ambion® In Vivo pre-designed siRNA (Life Technologies) against *Tmem135* (s91285) or *in vivo* negative control #1 siRNA (catalog 4459405) were complexed with Invivofectamine® 3.0 reagent (Life Technologies) according to manufacturer recommendations. The siRNA complexes were delivered via a 200 µl tail-vein injection at a final siRNA concentration of 1 mg/kg body weight. Mice were weighed prior to siRNA injection and again before euthanization. Mice were euthanized 4 days after siRNA injection at 4 hours after lights on, with or without a preceding 12 hour fast. Serum, liver, heart, adipose, and skeletal muscle were collected and snap frozen. Tissues were powdered while frozen and stored at -80° C until used.

Serum Analytes

Total cholesterol, HDL cholesterol, and triglyceride concentrations in serum were determined as we have described previously (Jensen et al., 2017). Briefly, the HDL fraction of serum was isolated by mixing serum 1:1 with 15% polyethylene glycol, centrifuging at 2,000 × g for 10 minutes at room temperature, and harvesting the HDL-containing supernatant. The cholesterol concentrations in whole serum and the HDL fraction were determined by a fluorometric enzyme assay consisting of cholesterol esterase (0.3 units/ml), cholesterol oxidase (1 unit/ml), horse radish peroxidase (1 unit/ml), and Amplex UltraRed® (50 µM, Life Technologies) in assay buffer (0.1 M potassium phosphate, pH 7.0, 50 mM NaCl, 5 mM cholic acid, 0.1% Triton X-100). The cholesterol assay was incubated at 37°C for 30 minutes, and fluorescence measured

in a Synergy H1 plate reader at 555 nm excitation and 585 nm emission wavelengths. Triglyceride concentrations in whole serum were determined using the same assay described earlier for HepG2 and mouse liver samples. Commercial enzymatic assays were used to quantify serum concentrations of β-hydroxybutyrate (BHB) (Cayman Chemical, catalog 700190), non-esterified fatty acids (NEFA) (Catachem Inc., catalog C514-0A), glucose (Pointe Scientific, Inc., catalog G7521), and a commercial ELISA was used to quantify serum insulin (Mercodia AB, catalog 10-1247) according to manufacturer recommendations.

Liver Analytes

Commercial kits were used for the extraction and quantification of liver NAD+ and NADH (Abcam Inc., catalog ab176723), and glycogen (BioAssay Systems, catalog E2GN), according to manufacturer recommendations. Concentrations of ATP and NEFAs in liver were determined as we have described elsewhere (Geisler et al., 2016). Briefly, for ATP determination frozen powdered liver was homogenized in ATP releasing agent (Sigma Chemical Co., catalog FLSAR). ATP was quantified with a luminescent ATP Determination Kit (Life Technologies, catalog A22066) and normalized to tissue weight. For NEFAs, powdered liver was sonicated in PBS as described earlier, and 100 µl lysate was mixed with 1 ml of 100% ethanol. Samples were vortexed for 10 minutes, centrifuged at 16,000 × g for 5 minutes, and the supernatant recovered. A commercial colorimetric assay for NEFAs (Catachem Inc., catalog C514-0A) was used and standards were diluted in ethanol, and NEFA concentrations were expressed on an equal protein basis.

To quantify ketones (BHB and acetoacetate), powdered liver was sonicated in PBS, acidified with 10% (*w:v*) trichloroacetic acid, centrifuged to remove proteins, and the supernatant was recovered and neutralized. Concentrations of BHB in the extract were determined using the same enzymatic assay described for serum. Concentrations of acetoacetate were determined using a modified assay based on methods described previously (Salway, 1969; Walker, 1954). Briefly, samples and standards were divided with one portion subjected to boiling (100° C for 5

minutes) to degrade acetoacetate, with the remaining portion kept on ice. A three-fold volume of freshly prepared diazo reagent (Walker, 1954) was then added to all samples and incubated at room temperature in the dark for 30 minutes. The reaction was stopped by adding a 20% volume of 2*N* NaOH, and absorbance was measured at 480 nm. The absorbance from the boiled sample was subtracted from the respective non-boiled sample, and acetoacetate concentrations were calculated from the resultant standard curve. Concentrations of cholic acid in liver were quantified using a competitive enzyme immunoassay according to manufacturer recommendations (Cell Biolabs, Inc., catalog MET-5007).

Liver Subcellular Fractionation

Powdered liver (approximately 50 mg) was homogenized for 40 strokes in a glass dounce homogenizer with a tight-fitting pestle using 600 µl of cold fractionation buffer (10 mM Tris-HCl, pH 7.4, 1 mM EGTA, 200 mM sucrose, protease and phosphatase inhibitor cocktail) on ice. The homogenate was transferred to a new tube, and the dounce homogenizer was washed with an additional 600 µl of fractionation buffer and transferred to the same tube. The homogenate was centrifuged at 600 × g for 10 minutes at 4°C to pellet unbroken cells and nuclei, and the supernatant transferred to a new tube. This low speed spin was repeated once more. Mitochondria and peroxisomes were pelleted by centrifugation at 7,000 × g for 10 minutes, and the supernatant (cytosolic fraction) was transferred to a new tube. The pellet was washed with 300 µl fractionation buffer and pelleted as before. The pellet was resuspended in 500 µl of fractionation buffer and a 30 µl aliquot was pelleted and solubilized in RIPA buffer for a BCA protein assay. Following protein assay mitochondria/peroxisome fractions were partitioned into 30 µg (protein content) aliquots followed by centrifugation and removal of the supernatant, and the pellets were frozen at -80°C.

Proteomic Analyses

The mitochondria/peroxisome-enriched fraction from a subset of fed control and TMEM135 knockdown mice was solubilized in RIPA buffer, proteins were precipitated with

acetone, and proteins were sent to the Arizona Proteomics Consortium for mass spectrometry identification of proteins. Proteins were digested with trypsin and equal quantities of protein (500 ng) were loaded. Samples were analyzed on a Thermo Q Exactive Plus Orbitrap mass spectrometer. Peptide identification in the resultant tandem mass spectra was performed using Proteome Discoverer Software version 1.3.0.339 scanning with the SEQUEST algorithm against the mouse proteome database (Mouse_unitprotkb_proteome_2016_0720_cont.fasta). Data analysis was performed using Scaffold version 4.8.1, with a peptide identification threshold of 95.0% and a minimum protein identification threshold of 99.9% and 2 unique peptides.

Western Blot

All primary antibodies were obtained from Abcam unless otherwise indicated. Catalog numbers and final concentrations or dilutions of each antibody were: rabbit polyclonal anti-ACAA1 (catalog ab154091, 1 µg/ml), rabbit monoclonal anti-ACOX1 (catalog ab184032, 1:2500 dilution), rabbit monoclonal anti-CAT (catalog ab209211, 1:2000 dilution), rabbit monoclonal anti-SCP2 (catalog ab140126, 1:2500 dilution), rabbit polyclonal anti-TMEM135 (catalog ab167096, 1 µg/ml), rabbit monoclonal anti-COX4I1 (Li-COR Inc., catalog 926-42214, 1:1000 dilution), mouse monoclonal anti-COX4I1 (catalog 14744, 0.25 µg/ml), mouse monoclonal anti-TUBB (Sigma Aldrich catalog T8328, 0.5 µg/ml), and rabbit polyclonal anti-PMP70 (catalog ab3421, 0.5 µg/ml).

Proteins (12.5 µg/well) were resolved on 4-12% Bis-Tris gels (Life Technologies) and subsequently transferred to nitrocellulose membranes. The membranes were blocked with 5% non-fat dry milk (NFDM) (*w:v*) in TBS with 0.1% (*v:v*) Tween (TBST) for 1 hour at room temp. All primary antibodies were diluted in TBST with 1% NFDM and incubated with the membranes on a rocking platform at 4° C overnight. The membranes were washed 4x with TBST, and IRDye® 680RD or 800CW-conjugated secondary antibodies (LI-COR Biosciences, Inc.) were diluted 1:4000 in TBST + 1% NFDM and incubated with membranes for 1 hour at room temp. The membranes were washed as before. Imaging and densitometry were performed with a Li-COR Odyssey CLx and Image Studio version 3.1 software, respectively.

Gas Chromatography (GC)

Lysates were prepared by sonicating frozen powdered liver in PBS as described earlier. Insoluble material was pelleted by centrifugation at 600 × g for 5 minutes. A BCA protein assay was performed on the cleared lysate. A one-step transesterification reaction was performed (Masood et al., 2005). Briefly, 1.7 ml of acidic methanol (1.6 ml methanol and 100 µl acetyl chloride) was added to borosilicate glass tubes with Teflon-lined caps. Butylated hydroxytoluene (BHT, 50 µg/ml) was added to methanol to prevent fatty acid oxidation. Tridecanoic acid (13:0, Cayman Chemical) was used as an internal standard because preliminary studies determined that it was not present in liver lysates. Tridecanoic acid was diluted in methanol/BHT to 100 µg/ml, and 100 µl was added to all samples and standards. Authentic standards for the following fatty acids were obtained from Cayman Chemical: 12:0, 14:0, 16:0, 16:1, 18:0, 18:1 cis(n9), 18:2 cis(n6), 20:3 cis(n6), 20:4 (n6), 22:0, 22:6 (n3), 24:0, 24:1, and 26:0. Pooled mixtures containing increasing concentrations of these fatty acids were prepared and dissolved in chloroform. 100 µl of authentic standards were added to standard tubes, and 100 µl of chloroform was added to unknown tubes. Next, 100 µl PBS was added to standard tubes, and 800 µg (protein content) of lysate diluted to a 100 µl volume with PBS was added to unknown tubes. The tubes were tightly capped and vortexed for 1 minute, and then incubated in a heating block at 100°C for one hour. The tubes were cooled to room temperature, 750 µl hexane was added and the tubes were vortexed for 30 seconds, and the upper organic layer was transferred to a GC sample vial. The hexane extraction was repeated once more. Hexane extracts were evaporated under a gentle stream of nitrogen to dryness and dissolved in 50 µl hexane.

GC was performed on an Agilent Technologies 6890N GC equipped with a Varian CP-Sil 88 column for fatty acid methyl ester analysis (100 m × 0.25 mm inner diameter × 0.2 µm film thickness) and a flame ionization detector. Inlet temperature was 250° C, and 1 µl of each standard or unknown was manually injected at a split ratio of 7.5:1. Helium was used as carrier gas at a 1.0 ml/minute constant flow. The oven was programmed for an initial temperature of 80°

C with a 4° C/min ramp to 220° C, a 5-minute hold, then a 4° C/min ramp to 240° C followed by a 10-minute hold. The detector was set at 270°C using air (450 ml/minute) and hydrogen (40 ml/minute), and nitrogen was used as make-up gas (10 ml/minute constant flow). The sampling frequency was 20 Hz.

OpenLAB CDS ChemStation Edition software version C.01.06 (Agilent Technologies) was used to analyze GC data. Retention times of authentic standards were matched with corresponding peaks in unknown samples. For each fatty acid, the peak area for standards and unknowns was divided by the internal standard peak area. The normalized peak area from increasing concentrations of authentic standards was plotted, and the R^2 for the resultant standard curves were > 0.995 in all cases. All fatty acids except 12:0 and 26:0 were identified in the unknowns, and fatty acid concentrations were determined by extrapolating the normalized peak area from the respective standard curve. Concentrations were expressed on an equal protein basis.

QUANTIFICATION AND STATISTICAL ANALYSIS

Statistical analyses were performed using Stata Version 14 and all differences were considered significant at $p< 0.05$. Information on the sample size, mean and error estimates, and indicators of statistical significance are presented in the figures and their corresponding legends. For immortalized cell lines, the total sample size (n) corresponds to cells on a different passage number and/or experiments performed on different days. Time course data in immortalized cell lines were analyzed by mixed effects regression analysis to account for repeated measures. Treatments were coded 0 or 1, and hours post-treatment and treatment × time interaction were included as fixed effects in the regression model with experimental replicate as the random effect. Differences between treatments at each timepoint were determined from the treatment × time interaction coefficient. For all other comparisons involving more than 2 groups, mixed effects regression analysis was performed using treatment as the fixed effect and experimental replicate as the random effect to account for repeated measures. Pairwise differences between treatments

were then determined using the Bonferroni multiple comparison method to control for the type 1 error rate. For comparisons involving only 2 groups, a paired t-test was performed.

For all mice data, the sample size refers to the number of mice. Regression analysis was used for mice outcomes except where indicated otherwise. Samples were coded 0 or 1 for fasting, TMEM135 knockdown fed mice, and TMEM135 knockdown fasted mice. The regression model utilized fasting, TMEM135 knockdown in the fed state, and TMEM135 knockdown in the fasted state, as predictors. The fasting coefficient indicated the difference due to fasting in control mice only, while the TMEM135 knockdown coefficients indicated the difference between control mice and TMEM135 knockdown mice within the fed state or fasted state. Differences were considered significant at $p < 0.05$, with p values ≥ 0.05 and < 0.10 considered trends. Only fed mice were used in proteomic analysis. Because the proteomic data does not follow a normal distribution due to some proteins not being detected in all samples, significant differences in proteomic data were determined from weighted spectra using the non-parametric Fisher's Exact test ($p < 0.05$) contained within the Scaffold version 4.8.1 software. The list of proteins that were significantly reduced in knockdown livers was further trimmed by hand to exclude proteins that were not detected in all the samples from mice that received the control siRNA.

Figure 1

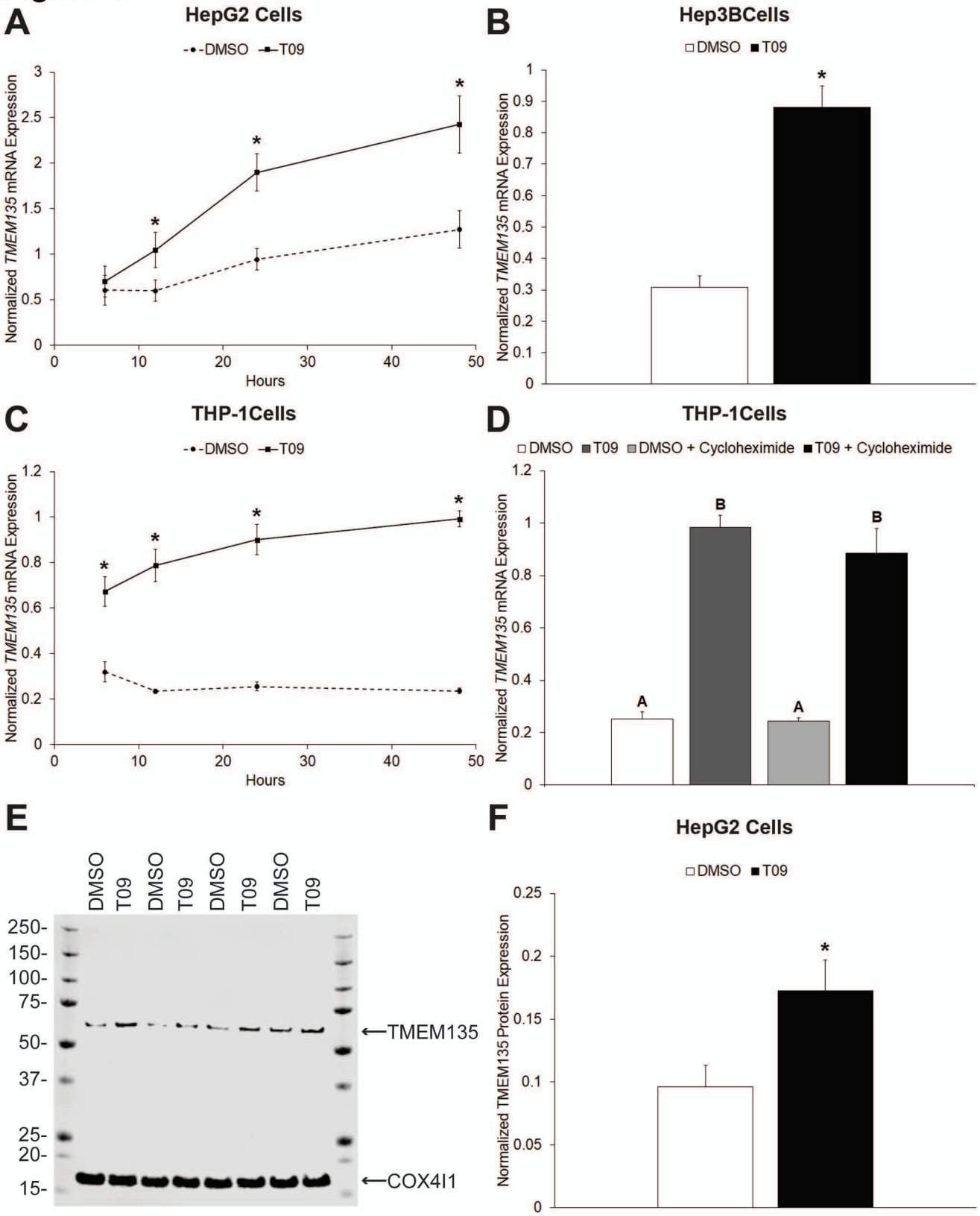
A
HepG2 Cells
DMSO
T09
Normalized TMEM135 mRNA Expression
Hours
B
Hep3BCells
DMSO
T09
Normalized TMEM135 mRNA Expression
C
THP-1Cells
DMSO
T09
Normalized TMEM135 mRNA Expression
Hours
D
THP-1Cells
DMSO
T09
DMSO + Cycloheximide
T09 + Cycloheximide
Normalized TMEM135 mRNA Expression
A
B
A
B
E
DMSO
T09
DMSO
T09
DMSO
T09
DMSO
T09
250-
150-
100-
75-
50-
37-
25-
20-
15-
TMEM135
COX4I1
F
HepG2 Cells
DMSO
T09
Normalized TMEM135 Protein Expression

Figure 2

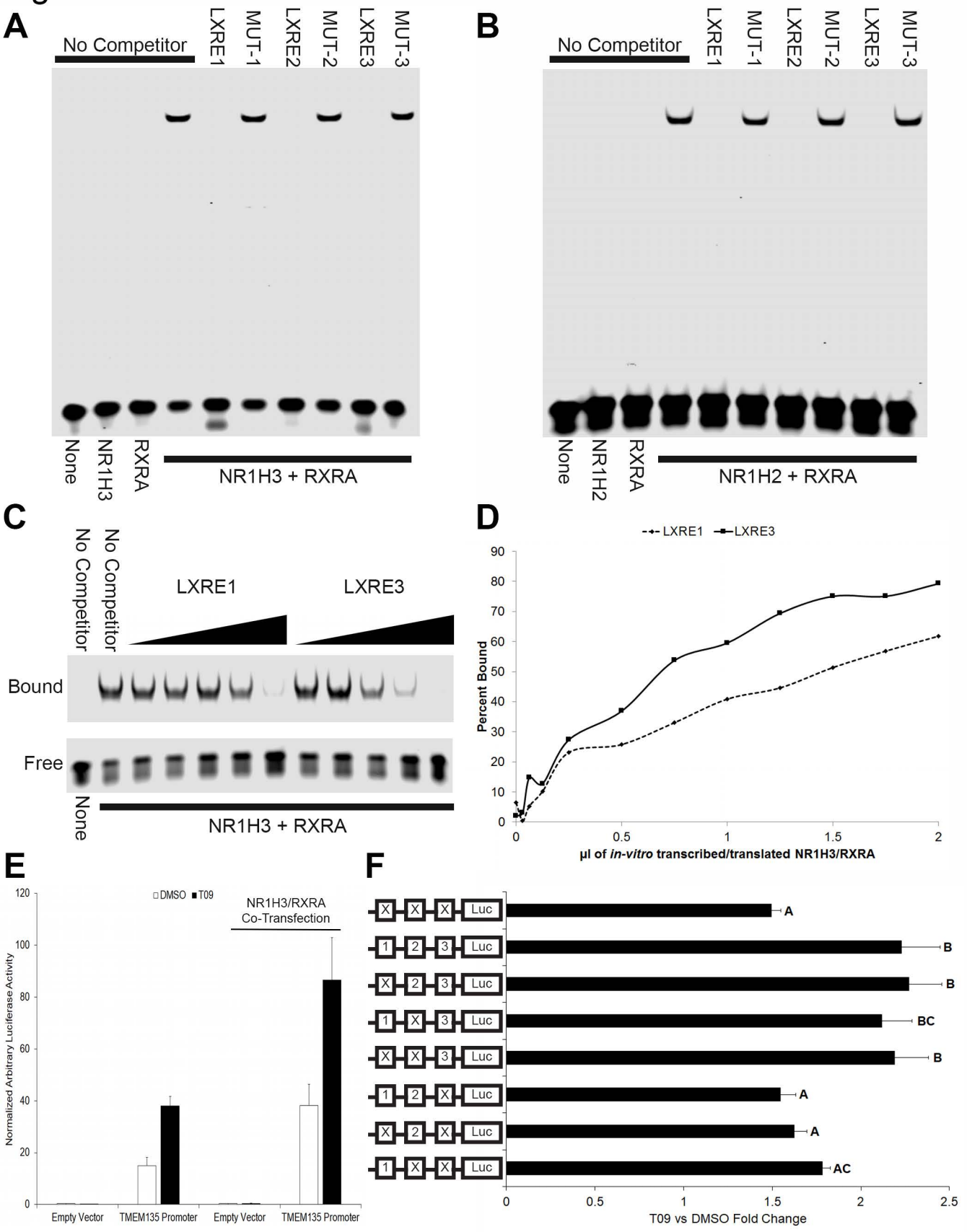
A
No Competitor
LXRE1
MUT-1
LXRE2
MUT-2
LXRE3
MUT-3
None
NR1H3
RXRA
NR1H3 + RXRA
B
No Competitor
LXRE1
MUT-1
LXRE2
MUT-2
LXRE3
MUT-3
None
NR1H2
RXRA
NR1H2 + RXRA
C
No Competitor
No Competitor
LXRE1
LXRE3
Bound
Free
None
NR1H3 + RXRA
D
LXRE1
LXRE3
Percent Bound
0
10
20
30
40
50
60
70
80
90
0
0.5
1
1.5
2
µl of *in-vitro* transcribed/translated NR1H3/RXRA
E
DMSO
T09
NR1H3/RXRA
Co-Transfection
Normalized Arbitrary Luciferase Activity
0
20
40
60
80
100
120
Empty Vector
TMEM135 Promoter
Empty Vector
TMEM135 Promoter
F
X X X Luc
A
1 2 3 Luc
B
X 2 3 Luc
B
1 X 3 Luc
BC
X X 3 Luc
B
1 2 X Luc
A
X 2 X Luc
A
1 X X Luc
AC
0
0.5
1
1.5
2
2.5
T09 vs DMSO Fold Change

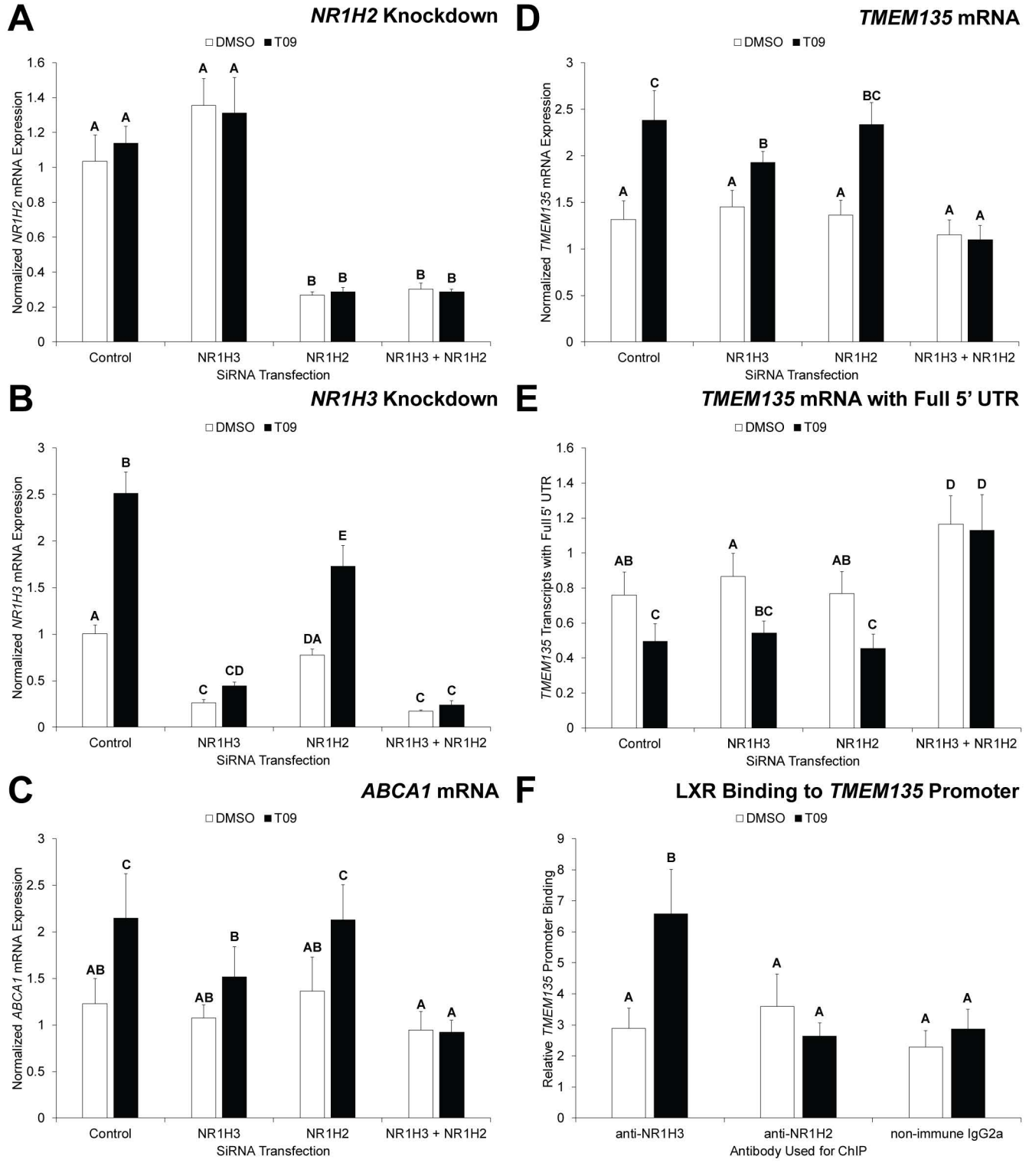
A
NR1H2 Knockdown
DMSO
T09
Normalized NR1H2 mRNA Expression
Control
NR1H3
NR1H2
NR1H3 + NR1H2
SiRNA Transfection
B
NR1H3 Knockdown
Normalized NR1H3 mRNA Expression
C
ABCA1 mRNA
Normalized ABCA1 mRNA Expression
D
TMEM135 mRNA
Normalized TMEM135 mRNA Expression
E
TMEM135 mRNA with Full 5' UTR
TMEM135 Transcripts with Full 5' UTR
F
LXR Binding to TMEM135 Promoter
Relative TMEM135 Promoter Binding
anti-NR1H3
anti-NR1H2
non-immune IgG2a
Antibody Used for ChIP

Figure 3

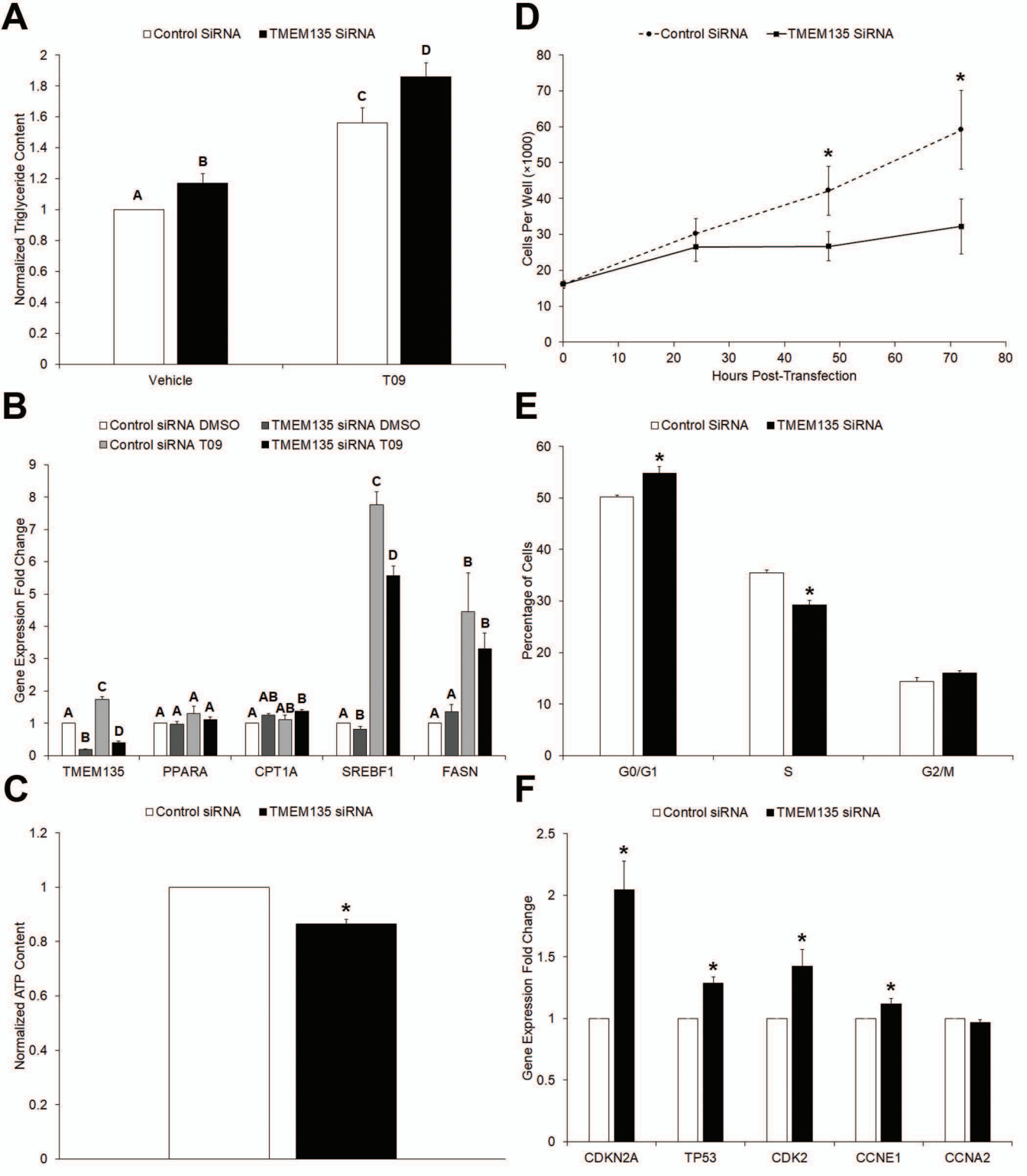
A
Control SiRNA
TMEM135 SiRNA
Normalized Triglyceride Content
Vehicle
T09
B
Control siRNA DMSO
TMEM135 siRNA DMSO
Control siRNA T09
TMEM135 siRNA T09
Gene Expression Fold Change
TMEM135
PPARA
CPT1A
SREBF1
FASN
C
Control siRNA
TMEM135 siRNA
Normalized ATP Content
D
Control SiRNA
TMEM135 SiRNA
Cells Per Well (×1000)
Hours Post-Transfection
E
Control SiRNA
TMEM135 SiRNA
Percentage of Cells
G0/G1
S
G2/M
F
Control siRNA
TMEM135 siRNA
Gene Expression Fold Change
CDKN2A
TP53
CDK2
CCNE1
CCNA2

Figure 4

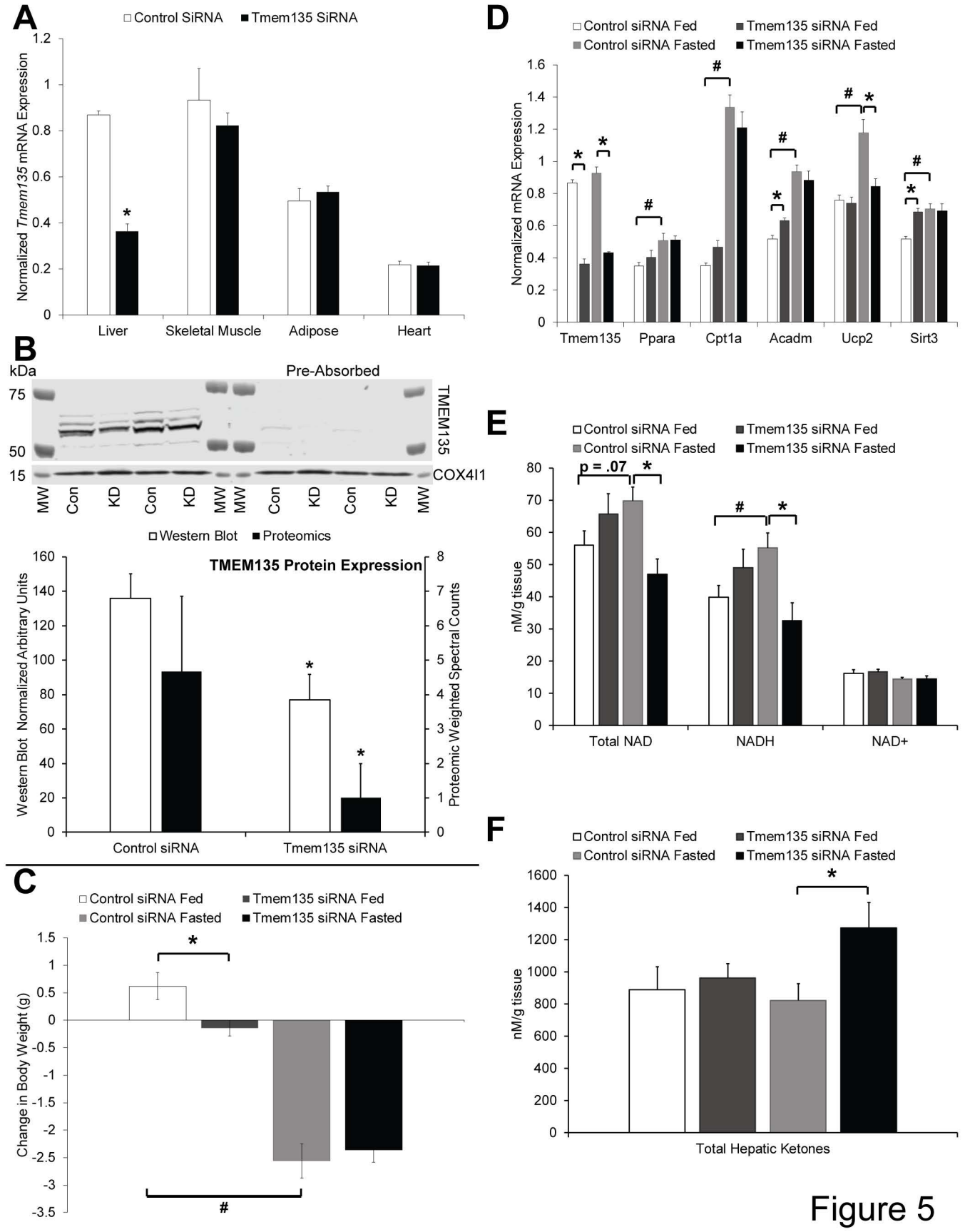
A
Control SiRNA
Tmem135 SiRNA
Normalized Tmem135 mRNA Expression
Liver
Skeletal Muscle
Adipose
Heart
B
kDa
Pre-Absorbed
75
50
15
TMEM135
COX4I1
MW
Con
KD
Con
KD
MW
MW
Con
KD
Con
KD
MW
Western Blot
Proteomics
TMEM135 Protein Expression
Western Blot Normalized Arbitrary Units
Proteomic Weighted Spectral Counts
Control siRNA
Tmem135 siRNA
C
Control siRNA Fed
Tmem135 siRNA Fed
Control siRNA Fasted
Tmem135 siRNA Fasted
Change in Body Weight (g)
D
Control siRNA Fed
Tmem135 siRNA Fed
Control siRNA Fasted
Tmem135 siRNA Fasted
Normalized mRNA Expression
Tmem135
Ppara
Cpt1a
Acadm
Ucp2
Sirt3
E
Control siRNA Fed
Tmem135 siRNA Fed
Control siRNA Fasted
Tmem135 siRNA Fasted
p = .07
nM/g tissue
Total NAD
NADH
NAD+
F
Control siRNA Fed
Tmem135 siRNA Fed
Control siRNA Fasted
Tmem135 siRNA Fasted
nM/g tissue
Total Hepatic Ketones

Figure 5

A

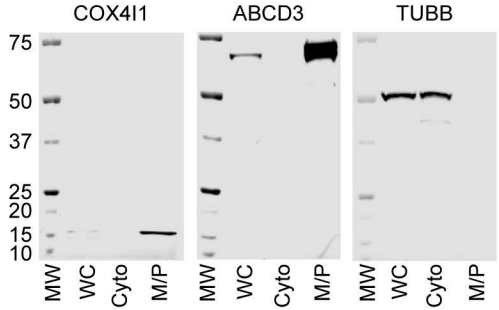

B

Protein Symbol	Weighted Spectral Counts ± SEM	
	Control siRNA	*Tmem135 siRNA*
CPS1	110 ± 16.3	84.7 ± 34.1
CAT	125 ± 7.6	76 ± 14
SCP2	128 ± 13.1	69.7 ± 35.3
HSD17B4	66 ± 8.5	46.7 ± 9.5
CES1	61.3 ± 11.8	43.3 ± 7.2
NUDT7	28 ± 8.2	17 ± 17
ACOX1	27 ± 6.7	13 ± 10.5
PC	24.3 ± 3.8	15.7 ± 4.7
ACOX2	22 ± 4.4	13.3 ± 11.9
CES3	17.7 ± 3.7	10.7 ± 6.1
GLUD1	21 ± 2.3	13 ± 3.1
DHRS4	23.3 ± 3.4	11.3 ± 6.4
HACL1	20.7 ± 3.7	9.7 ± 5.7
COMT	17.7 ± 5.8	8.3 ± 8.3
MTTP	15 ± 4.7	7.7 ± 4.3
PSAP	14 ± 4.5	5.3 ± 3.2
ACAA1	35 ± 6.5	9.3 ± 9.3
ALDH3A2	11 ± 2.9	5.3 ± 3.5
ALDH6A1	11 ± 2.9	5.7 ± 3.5
AMACR	10 ± 2.6	4 ± 4
SUCLA2	9 ± 1.7	3.3 ± 2.4
ACADL	5 ± 0.6	1.7 ± 0.9
SLCO1A1	3.7 ± 1.2	1 ± 1

C

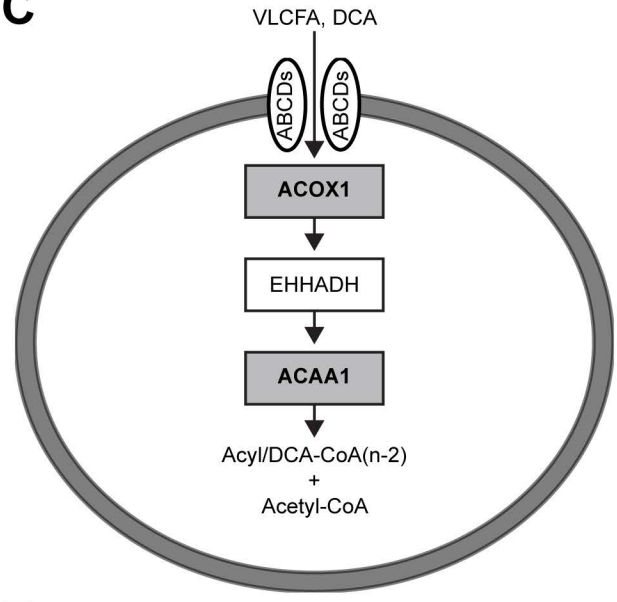

D

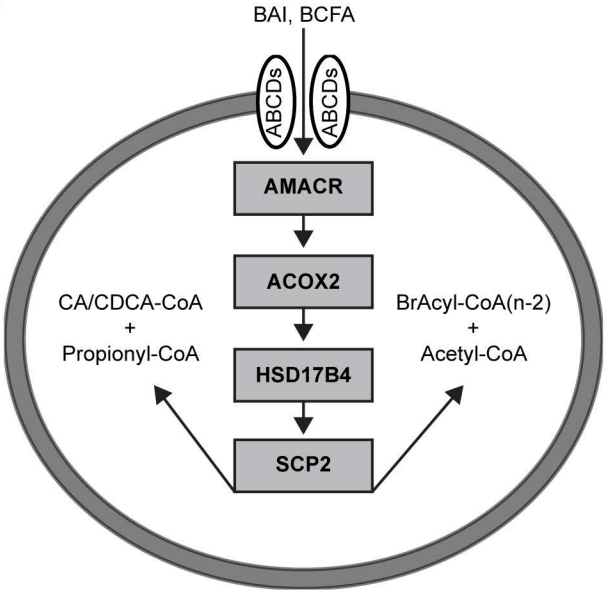

E

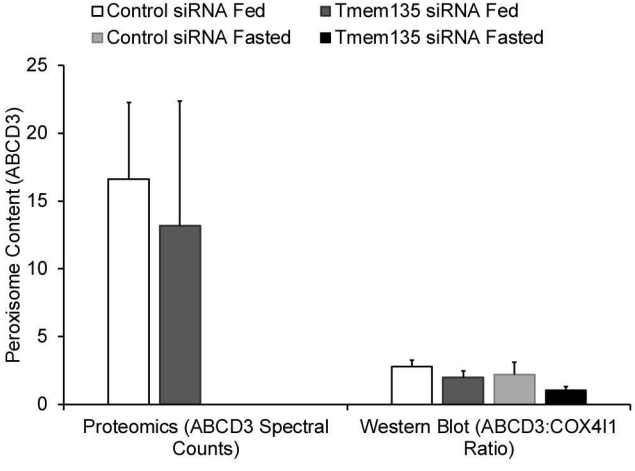

F

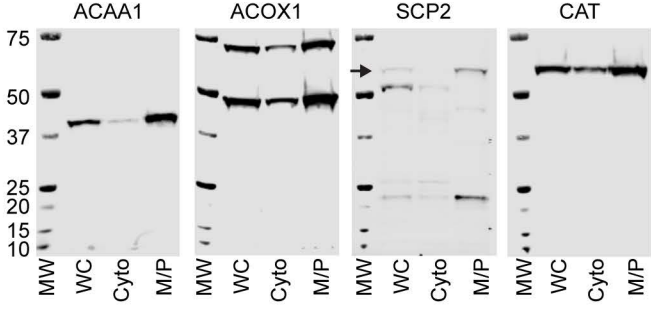

Figure 6

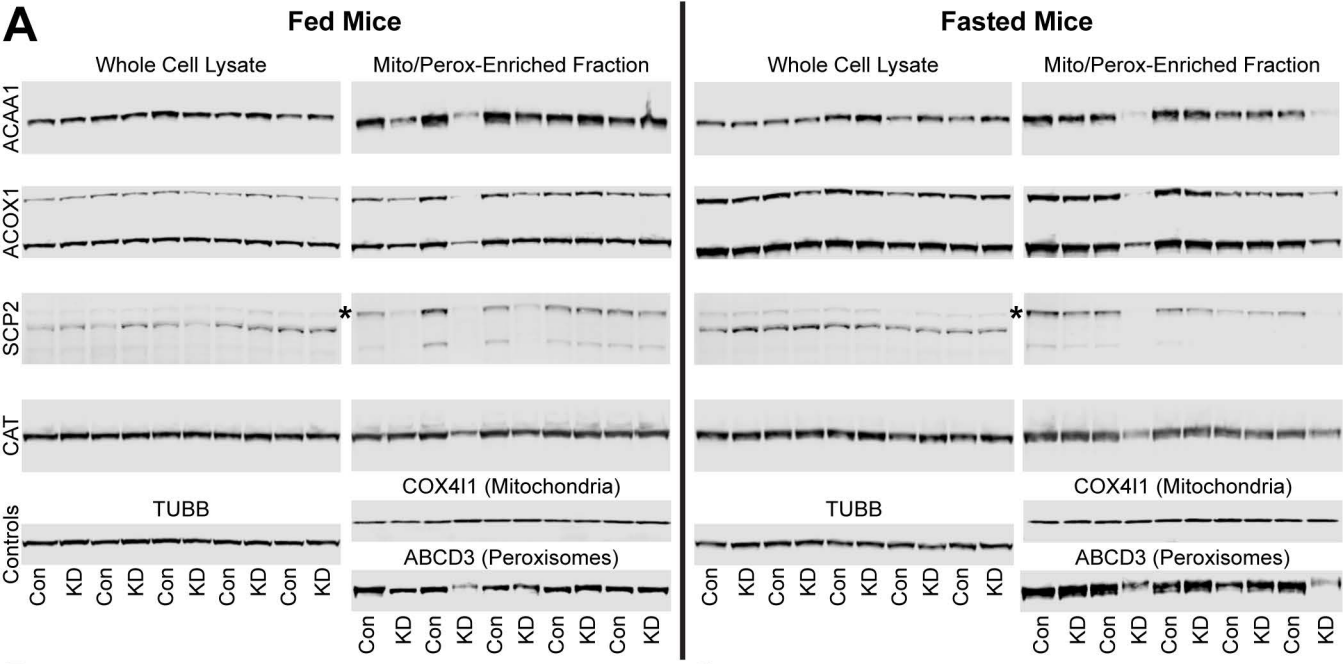

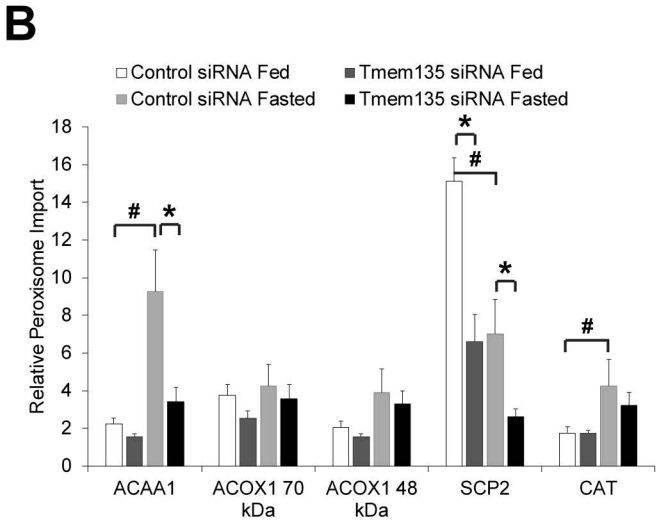

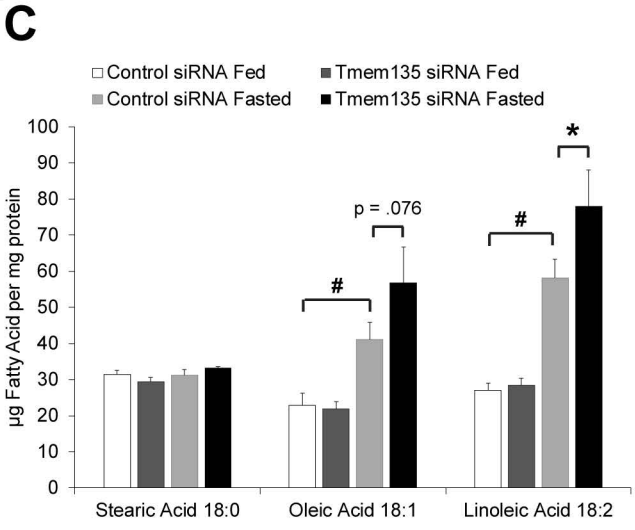

D

Fatty Acids

	Fed Mice			Fasted Mice		
	Control siRNA	*Tmem135 siRNA*	*P*	*Control siRNA*	*Tmem135 siRNA*	*P*
14:0	0.32 ± 0.06	0.29 ± 0.03		0.73 ± 0.12 #	0.85 ± 0.18	
16:0	48.9 ± 3.6	45.7 ± 2.2		70.2 ± 4.4 #	83.1 ± 7.5	^
16:1	2.4 ± 0.5	2.2 ± 0.2		3.5 ± 0.7	5.3 ± 1.0	^
18:0	31.3 ± 1.3	29.4 ± 1.2		31.3 ± 1.6	33.2 ± 0.4	
18:1	22.9 ± 3.4	22.0 ± 1.9		41.1 ± 4.8 #	56.7 ± 9.9	^
18:2	27.1 ± 2.0	28.5 ± 1.9		58.1 ± 5.1 #	78.0 ± 10.0	*
20:3	2.2 ± 0.2	2.1 ± 0.2		1.1 ± 0.1 #	1.6 ± 0.1	^
20:4	21.0 ± 1.6	19.2 ± 1.4		20.8 ± 1.1	23.4 ± 0.7	
22:0	1.7 ± 0.1	1.4 ± 0.1	*	1.4 ± 0.1	1.6 ± 0.1	
22:6	13.0 ± 1.2	11.7 ± 1.0		17.1 ± 1.1 #	19.0 ± 0.9	
24:0	1.01 ± 0.03	0.83 ± 0.05	^	0.95 ± 0.08	1.01 ± 0.05	
24:1	0.87 ± 0.04	0.87 ± 0.05		1.0 ± 0.1	1.19 ± 0.06	^
Total	172.5 ± 12.9	164.1 ± 7.7		247.4 ± 14.2 #	304.8 ± 28.3	*

Figure 7